



Electrochemical reduction of CO₂ and CO using interface-engineered Au/Ti electrodes for long-chain hydrocarbon production

Young Jun Kim, Ju Young Maeng, Seon Young Hwang, Choong Kyun Rhee, Youngku Sohn^{*}

Department of Chemistry, Chungnam National University, Daejeon 34134, Republic of Korea

ARTICLE INFO

Keywords:

Au/Ti interface
Electrochemical CO₂ reduction
Electrochemical CO reduction
Fischer–Tropsch synthesis
Long chain hydrocarbons

ABSTRACT

This study demonstrates the electrochemical reduction of CO₂ and CO using interface-engineered Au/Ti electrodes. Direct adsorption of CO and indirect processes in CO₂ conditions were proposed to form surface CO. Surface H was formed from H⁺/H₂O. Mimicking Fischer–Tropsch synthesis between surface CO and H resulted in the production of CH₄ and hydrocarbons (C_nH_{2n} and C_nH_{2n+2}, n = 2–7). Faradaic efficiency of CO increased with increasing Au coverage and reached 38%. In CO₂-saturated KHCO₃, long-chain hydrocarbon production was observed on Au/Ti electrodes with low Au coverage. In CO₂ and CO-saturated phosphate electrolytes, higher Au coverage resulted in higher production of long-chain hydrocarbons. The ratio of alkanes to alkenes increased with increasing Au coverage but decreased with applied potential. The study provides insights into interface engineering, electrochemical long-chain hydrocarbon production, and C–C coupling mechanisms.

1. Introduction

CO₂ recycling has become a reliable strategy in industry to address both energy and environmental challenges, and the electrochemical CO₂ reduction (EC-CO₂R) method has been extensively employed to achieve this goal [1–10]. While Cu-based electrodes have been extensively studied [11–15], new hybrid electrocatalysts have also been developed and tested to improve stability and selectivity towards specific products [1–10]. Among the hybrid catalysts, gold (Au) and TiO₂ have been employed and extensively tested in photocatalytic CO₂ reduction (PC-CO₂R) [16–25], but there have been relatively fewer studies on their performance in EC-CO₂R [26–28]. Hossain et al. reported the formation of diverse products, including CO, CH₄, HCOO[−], CH₃COO[−], methanol, and ethanol, during EC-CO₂R over TiO₂/Au nanocomposites prepared by Zn galvanic replacement, using 0.1 M NaHCO₃ electrolyte [26]. Liu et al. reported that during photoelectrochemical (PEC) CO₂ reduction using Au-coated TiO₂/InP nanoparticles, the major products were H₂ and CO, with an FE of 84.2% for CO achieved at −0.11 V (vs. RHE) in a 0.1 M KHCO₃ electrolyte [27]. The CO/H₂ ratio was reported to be controlled from 0.27 to 6.1 by interface engineering of Au and TiO₂ in PEC-CO₂R. It is known that Au is selective to CO in EC-CO₂R [29–32], while TiO₂ is a hydrogen production electrocatalyst [33–35]. Therefore, in the hybrid TiO₂/Au system, it is plausible that surface CO and H are formed on the surface. Subsequently, these species can be manipulated

to form hydrocarbons at the interface. The conventional Fischer–Tropsch (F–T) synthesis, which involves reactions of ((2 n + 1)H₂ + nCO → C_nH_{2n+2} + nH₂O and 2nH₂ + nCO → C_nH_{2n} + nH₂O), is commonly performed at high pressure and high temperature conditions [36,37]. Further, syngas for this synthesis has traditionally been derived from natural gas and coal, making conventional F–T methods environmentally unfriendly. Multicarbon long-chain hydrocarbons can be synthesized at ambient temperature and pressure conditions by using CO₂ (or CO through electrochemistry) in a mimicked EC F–T process. As a result, this energy-efficient process requires less energy. The formation of multicarbon (C₂₊) compounds in EC-CO₂R requires C–C coupling, which is essential for the reaction mechanism. The coupling of intermediate species such as *CO, *CHO, and *COH has been extensively studied and discussed in previous works [11–15,38,39]. Previous studies have extensively discussed the formation of C₂H₄ and oxygenated hydrocarbons such as ethanol, acetate, and propanol, utilizing both experimental and theoretical approaches. However, studies focused on the production of longer chain hydrocarbons such as series of C_nH_{2n+2} and C_nH_{2n} have been limited [40,41]. Although their Faradaic efficiencies (FEs) were observed to be low, the production pathway cannot be neglected for deeper understanding of C–C coupling and the development of electrocatalysts for long-chain hydrocarbons. Surface adsorbed CO can also be achieved by direct CO adsorption in CO-saturated electrolyte, and the hydrocarbons are also expected to be produced by EC CO reduction

^{*} Corresponding author.

E-mail address: youngkusohn@cnu.ac.kr (Y. Sohn).

<https://doi.org/10.1016/j.apcatb.2023.123017>

Received 15 March 2023; Received in revised form 21 May 2023; Accepted 16 June 2023

Available online 17 June 2023

0926-3373/© 2023 Elsevier B.V. All rights reserved.

(EC-COR) [42–45].

Motivated by these findings, an Au/Ti hybrid was chosen and tested in both EC CO₂ and CO reduction experiments. It was expected that a good interface would be formed between Au and Ti due to their strong interaction, which would remain stable during the electrochemical reaction [46]. Consequently, F-T synthesis like series of long chain C_nH_{2n+2} and C_nH_{2n} were found to be produced, including CO and H₂. Overall, the unique proposed idea and the results obtained are very useful for deeper understanding of C–C coupling mechanism and the development of electrocatalyst for C₂₊ products.

2. Experimental section

Preparation of Au/Ti electrodes was carried out as follows. Ti foils (0.1 mm thick, 99.9%, purchased from Aliexpress) were first polished using fine sandpaper and cleaned in deionized water via sonication. Au was then deposited onto the Ti foil using a SPT-20 ion DC sputtering coater (COXEM Co., Korea) with a 99.99 + % purity Au sputter target. The ionization current was set at 3 mA and deposition times of 10 s, 20 s, 80 s, 160 s, and 640 s were used, resulting in calibrated thicknesses of 0.5 nm, 1.0 nm, 3.8 nm, 7.7 nm, and 30.7 nm, respectively. Briefly, the vendor (COXEM Co., Korea) provided cross-sectional thickness data of Au on Si, obtained using a field-emission scanning electron microscope. The Au was deposited for 100 s, 200 s, and 300 s under the same 3 mA condition using a coater of the same model. We fitted the three data points and obtained the equation $y = 0.048 (\pm 4\%)x$, where y represents the thickness in nm and x denotes the Au deposition time at 3 mA in seconds. The thickness was obtained using the obtained equation. The as-prepared samples were designated as Au(sputter-time)/Ti, for example Au(10 s)/Ti. To investigate the effect of the Au/Ti interface, Au was also loaded onto a Ti support using the galvanic replacement method. A bare Ti foil (5 mm × 30 mm) was immersed in a 1 mM Au solution (using HAuCl₄·3 H₂O, ≥99.9%, Sigma-Aldrich) for 1 h, 2 h, 6 h, and 24 h to control the Au thickness. The results of electrochemical CO₂ reduction were compared with those obtained using sputter-deposited Au on Ti electrodes.

To confirm the crystalline status of Ti and Au(640 s)/Ti samples, X-ray diffraction patterns were obtained. A MiniFlex II X-ray diffractometer (Rigaku Corp., CNU Chemistry Core Facility center) was used with Cu Kα (40 kV and 30 mA) X-ray line. Surface morphologies of bare Ti and Au/Ti electrodes were examined before and after EC tests using a scanning electron microscope (SEM, S-4800, Hitachi, Ltd.). Energy-dispersive X-ray spectroscopy (EDXS) data and elemental mapping images were acquired using a Merlin Compact SEM from Carl Zeiss Co. Ltd., which was coupled with an AZtec Energy X-MaxN EDXS system provided by Oxford Instruments. The oxidation states and stability of the overlayer Au and Ti support were confirmed by employing X-ray photoelectron spectroscopy (XPS). A Thermo Scientific K-alpha⁺ XPS spectrometer equipped with a hemispherical energy analyzer and monochromated Al Kα X-ray (1486.7 eV) source was used. Ultraviolet photoelectron spectroscopy (UPS) was used to examine changes in the work function and density of states (DOS) near the Fermi level. The same Thermo Scientific K-alpha⁺ XPS spectrometer was used, but a He I light source of 21.22 eV was employed. During the UPS measurement, a sample bias of −10.0 V was applied to the sample.

For the EC CO₂ and CO reduction tests, a potentiostat/galvanostat (CHI 660D, CH Instruments) was used in the conventional three-electrode mode. Bare Ti and Au/Ti foils were cut to a size of 5 mm × 30 mm and used as the working electrode. A Pt wire and an Ag/AgCl (3.0 M KCl) were used as the counter and reference electrodes, respectively. The electrolytes were prepared using KHCO₃ (99.7%, Sigma-Aldrich), NaHCO₃ (99.7%, Sigma-Aldrich), K₂HPO₄ (99.0%, Junsei), and KH₂PO₄ (99.0%, Acros) as received. The electrolytes used were KHCO₃ (0.1 M, 0.2 M, and 0.5 M), 0.1 M NaHCO₃, and 0.1 M K₂HPO₄/KH₂PO₄ with a 50 mL volume. The EC cell size was 100 mL, and it was tightly sealed during the EC tests. CO₂ gas (99.99%) and CO gas

(99.95%) were fully bubbled into the electrolyte and charged in the EC cell for EC-CO₂R and EC-COR, respectively. Linear sweep voltammetry (LSV) was conducted from 0.0 V to −2.0 V (vs. Ag/AgCl) with a scan rate of 10 mV/s in N₂ and CO₂-saturated electrolytes. Amperometry tests were conducted at an applied potential between −1.4 V and −2.0 V (vs. Ag/AgCl) for 1 h. The potential versus reversible hydrogen electrode (RHE) was calculated using the following formula $V \text{ (vs. RHE)} = V \text{ (vs. Ag/AgCl)} + 0.197 + (0.0591 \times \text{pH})$. Electrochemical surface area (ECSA) measurements were performed on bare Ti, Au/Ti, and bare Au electrodes in a CO₂-saturated 0.1 M KHCO₃ electrolyte within the non-Faradaic potential range. Cyclic voltammetry (CV) curves were obtained at different scan rates within the range of −0.1 V to −0.4 V_{Ag/AgCl} for this purpose.

For the analysis of reduction gas products, a YL 6500 gas chromatograph (Young In Chromass Co., Ltd.) was used, which was equipped with a thermal conductivity detector, a flame ionization detector, and a Ni catalyst methanizer assembly. The GC had two injection ports, one for 40/60 Carboxen-1000 (which separated H₂, air, CO₂, CO, CH₄, C₂H₄, and C₂H₆) and the other for HP-Plot Q PT (which separated a series of C_nH_{2n+2} and C_nH_{2n}, n=3–7) columns. The HP-Plot Q PT column was first used with 0.5 mL of gas, followed by the other column with the remaining 0.5 mL of gas. A QP2010 GC-mass spectrometry (Shimadzu Corp.) was used to further confirm the series of alkanes (C_nH_{2n+2}) and alkenes (C_nH_{2n}) separated with a HP-Plot Q PT column. No hydrocarbon impurities were detected in the CO₂ and CO feed gases using GC analysis. Various GC peaks with different retention times were identified and quantified using calibrated gases. Two sets of calibrated mixed gases were used for quantifying the GC signals. The first set contained CH₄, C_nH_{2n+2}, and C_nH_{2n} gases with n = 2–5, each at a concentration of 100 μmol/mol in N₂ balance. The second set included H₂ (10,000 μmol/mol), N₂ (10,000 μmol/mol), O₂ (10,000 μmol/mol), CO (100 μmol/mol), C_nH_{2n+2} with n = 1,2 (100 μmol/mol), and C₂H₄ (100 μmol/mol), in Ar balance. No liquid reduction products were found, which was confirmed by nuclear magnetic resonance (NMR) spectroscopy. 0.5 mL of the liquid was analyzed using a 600 MHz FT NMR (AVANCE III, Bruker Corp.). We calculated the Faradaic efficiency (FE) of the detected gas product using the following equation: $\text{FE} = nZF/(I \times t)$, where Z represents the number of electrons for each product, F denotes the Faraday constant, I denotes the measured current (from the amperometry curve), t represents the reaction time, and n is the total amount of product (in moles) estimated from GC.

3. Results and discussion

3.1. EC CO₂ reduction tests over Au/Ti with in CO₂-saturated 0.1 M KHCO₃ electrolyte

3.1.1. Au thickness effects

The EC CO₂ reduction experiment was conducted using an Au/Ti electrode with an applied potential of −1.6 V (vs. Ag/AgCl) in a 0.1 M KHCO₃ electrolyte. The potential corresponds to −1.0 V (vs. RHE). The three electrode system and initial CO₂ and H⁺ adsorption processes are illustrated in Fig. 1a. Amperometry experiments were performed for 1 h at −1.6 V_{Ag/AgCl} over bare Ti and Au/Ti electrodes with varying Au deposition times (Fig. 1a1). The current density (CD, mA/cm²) (or total charge in the inset) increased with increasing Au deposition time, and remained relatively constant above 80 s. The amperometry curves showed similar profiles above 80 s, indicating a similar applied charge. LSV curves (negative going from 0 to −2.0 V) were obtained for selected bare Ti, Au(80 s)/Ti, and Au(640 s)/Ti electrodes in CO₂ and N₂-saturated electrolytes (Supporting Information, Fig. S1a). The results showed that the CD in the CO₂-saturated electrolyte was higher than that in the N₂-saturated electrolyte, suggesting that CO₂ reduction current was likely involved in the CD.

H₂ production was the major product for the bare Ti electrode, while CO production increased significantly with increasing Au thickness

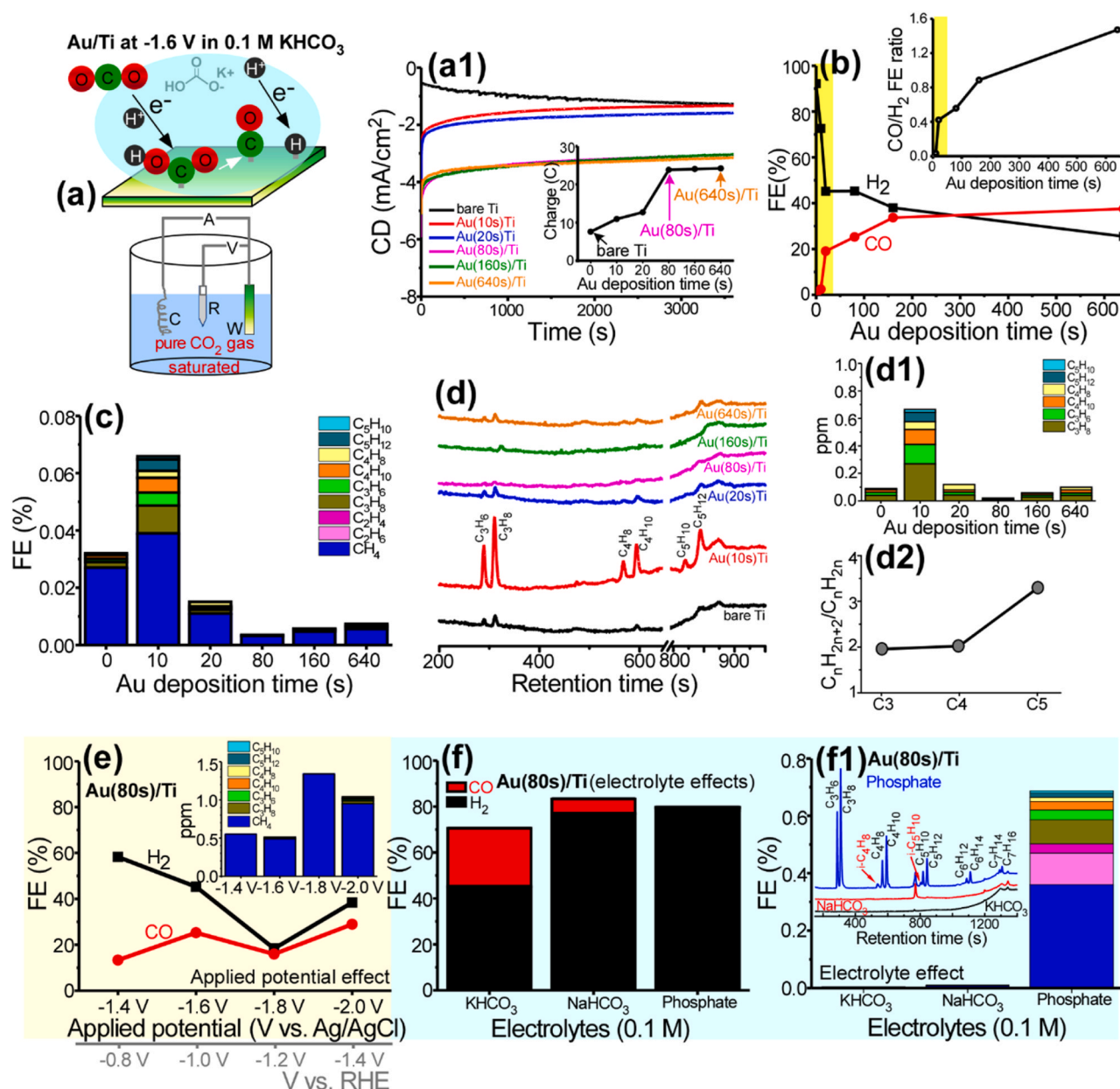


Fig. 1. Scheme for EC CO₂ reduction in CO₂-saturated 0.1 M KHCO₃ electrolyte (a). Amperometry i-t curves (corresponding charges in the inset) at -1.6 V_{Ag/AgCl} over bare Ti and Au/Ti electrodes (a1). FEs of CO and H₂ products, and the CO/H₂ ratio in the inset (b). FEs of CH₄ and C₂₋₅ compounds (c). GC profiles separated by HP-Plot Q PT column (d). Amounts of C₂₋₅ compounds (d1) and the corresponding C_nH_{2n+2}/C_nH_{2n} ratios (d2). FEs of CO and H₂ products over Au(80 s)/Ti at -1.4 V, -1.6 V, -1.8 V, and -2.0 V_{Ag/AgCl} in 0.1 M KHCO₃ electrolyte for 1 h (e). FEs of CO and H₂ products over Au(80 s)/Ti at -1.6 V_{Ag/AgCl} in 0.1 M KHCO₃, 0.1 M NaHCO₃, and 0.1 M phosphate buffer electrolytes for 1 h (f). FEs of CH₄ and C₂₋₅ compounds and the corresponding GC profiles in the inset (f1).

(Fig. S1b, b1, and Table S1). CO production over Au(640 s)/Ti was higher than the H₂ production amount. Consequently, in Fig. 1b, the FE of H₂ was observed to be approximately 92% for the bare Ti electrode and decreased with increasing Au thickness. On the other hand, the FE of CO was only 0.04% for the bare Ti electrode but dramatically increased with increasing Au thickness, reaching 37.5% for Au(640 s)/Ti. The resulting CO/H₂ FE ratio increased with increasing Au deposition time (inset of Fig. 1b). The Au(20 s)/Ti electrode exhibited a sharper decrease in H₂ production and an increase in CO production (or FEs). Under this interfacial condition, it was assumed that the active site for CO production became more prevalent while the sites for H₂ production decreased. Beyond 20 s, the FEs of H₂ and CO gradually changed with deposition time, as shown in Fig. 1b.

CH₄ FE was maximized to a level of 0.04% over Au(10 s)/Ti, while the other electrodes showed much lower (Fig. 1c). The CH₄ detection

amounts were only below 3 ppm (Fig. S1c). C₂H₄ and C₂H₆ were not detected in the GC profiles (Fig. S1d). Interestingly, C₃₋₅ hydrocarbons (C₃H₆, C₃H₈, C₄H₈, C₄H₁₀, C₅H₁₀, and C₅H₁₂) were detected, although the total amount was below 1 ppm (Fig. 1d and d1). The maximum FEs were observed over the Au(10 s)/Ti electrode (Fig. 1c). The total FE of C₃₋₅ hydrocarbons was about 0.03% (Fig. 1c). The FEs of CH₄ and C₃₋₅ hydrocarbons showed maxima over the Au(10 s)/Ti electrode. These results suggest that the interface effect was crucial for the production of hydrocarbons. For the C_nH_{2n+2}/C_nH_{2n} ratios of C₃₋₅ hydrocarbons over Au(10 s)/Ti (Fig. 1d2), the ratios were estimated to be between 2 and 4, indicating that alkanes were produced more than the corresponding alkenes.

3.1.2. Applied potential and electrolyte effects over Au(80 s)/Ti

The effects of applied potentials and electrolytes on Au(80 s)/Ti

electrode were examined. CD was increased in the range of 2–8 mA/cm² with increasing the potential (Fig. S2). The production amounts were commonly increased with increasing the potential due to an increase in CD (Fig. S2 and Table S2). The resulting FE of H₂ somewhat decreased at higher potential, but that of CO was increased at higher potential (Fig. 1e). The graph included the potential vs. RHE, but our main focus of discussion was on the potential vs. Ag/AgCl. The CO/H₂ ratio was maximized at $-1.8 \text{ V}_{\text{Ag/AgCl}}$ and somewhat decreased at $-2.0 \text{ V}_{\text{Ag/AgCl}}$. Similarly, the FE of CH₄ was maximized at $-1.8 \text{ V}_{\text{Ag/AgCl}}$ and decreased at $-2.0 \text{ V}_{\text{Ag/AgCl}}$ (inset of Fig. 1e). C_{3–5} hydrocarbons were observed to be more produced at $-2.0 \text{ V}_{\text{Ag/AgCl}}$, and their FEs were maximized at that potential (Fig. 1e and Fig. S2). The results for the bare Ti are presented in Fig. S3 and Table S3. These results confirmed that the introduction of an Au overlayer on the Ti support enhanced the production of C_{3–5} hydrocarbons. The FE for CO was negligibly small (< 0.1%) for bare Ti, but substantially increased upon introducing Au on Ti.

Different electrolytes (0.1 M) such as KHCO₃, NaHCO₃, and phosphate were tested at $-1.6 \text{ V}_{\text{Ag/AgCl}}$ over Au(80 s)/Ti electrode (Fig. 1f and f1, Fig. S4, and Table S4). The FE of H₂ was significantly increased in NaHCO₃ and phosphate electrolytes compared to that in 0.1 M KHCO₃ electrolyte. On the other hand, the FE of CO was substantially decreased to 6.2% and 0.6% in NaHCO₃ and phosphate, respectively (Fig. 1f). A more dramatic result was found in the productions of CH₄ and C_{2–7} hydrocarbons (Fig. 1f1). The FE of CH₄ was increased from 0.003% to 0.007% and 0.36% when 0.1 M KHCO₃ was replaced by 0.1 M NaHCO₃ and 0.1 M phosphate electrolytes, respectively. The C₂H₄, C₂H₆, and C_{3–7} hydrocarbons were almost undetectable in KHCO₃ and NaHCO₃ but drastically increased and observed in the phosphate electrolyte (Fig. 1f1). Isomers of i-C₄H₈ (isobutane), and i-C₅H₁₀ (isopentane) were clearly detected in the GC profiles. It appears that when neighboring H was more available on the electrode surface, hydrocarbon production was increased, discussed further below.

3.1.3. Recycling and N₂ condition tests over Au(80 s)/Ti electrode

Experiments were conducted to investigate the effects of recycling and CO₂-free conditions on the performance of the Au(80 s)/Ti electrode. For recycling tests under CO₂-saturated 0.1 M KHCO₃ electrolyte, the CD at $-1.6 \text{ V}_{\text{Ag/AgCl}}$ was found to increase with increasing cycling number (Fig. S5 and Table S5). Although H₂ production increased in the 2nd cycle, it decreased again in the 3rd cycle. CO production was substantially reduced with increasing recycling number. Interestingly, CH₄ and C_{3–5} hydrocarbons increased after recycling and reached their maximum levels in the 2nd cycle, while the CO/H₂ ratio was minimized. This suggests that the CO/H₂ ratio is closely related to hydrocarbon production, as previously observed. In addition, the Au(80 s)/Ti electrode was tested in both N₂ and CO₂-saturated 0.1 M KHCO₃ electrolyte conditions (Fig. S6 and Table S6). CD was slightly higher in the CO₂-saturated condition due to additional CO₂ reduction current. H₂ production was slightly higher in the N₂-saturated condition, while CO production was suppressed in N₂ due to the absence of a carbon source. This confirms that CO is produced via CO₂ adsorption.

3.1.4. Au//Ti electrode by the galvanic replacement

To further investigate the effect of the Au/Ti interface or thickness, Au was also loaded onto a Ti support using the galvanic replacement method (Fig. S7 and Table S7). The thickness of Au was controlled by varying the dipping time of the Ti in the Au solution (1 h, 2 h, 6 h, and 24 h). The FEs of H₂ and CO showed a gradual decrease and increase, respectively, with longer dipping times. The FE for CO reached its maximum, while that of H₂ was minimized at the 24 h dipping time. These results suggest that the Au thickness increased with longer dipping times. Interestingly, at the 2 h dipping time, we observed increased production of CH₄, C₂H₄, C₂H₆, and C_{3–5} hydrocarbons. C₂H₄ and C₂H₆ were almost not detected at the shorter (1 h) and longer (6 h) dipping times. The FEs of C_{2–5} hydrocarbons were maximized at the 2 h dipping time. However, at 6 h and 24 h dipping times, the production of

hydrocarbons drastically decreased. Although we did not characterize the Au/Ti interface by the galvanic replacement method in the demonstration tests, these results clearly demonstrate the significant influence of Au thickness (or Au/Ti interface) on hydrocarbon production.

3.2. Concentration effects on EC CO₂ reduction over Au(80 s)/Ti and Au(10 s)/Ti in CO₂-saturated KHCO₃ electrolyte

As discussed previously, the production of C_{3–7} hydrocarbons was almost undetectable in 0.1 M KHCO₃, leading to the conclusion that the presence of H⁺ ions was necessary for their production. To investigate this further, the concentration of KHCO₃ was increased to 0.2 M and 0.5 M, and the resulting CO₂ reduction products were examined using a selected Au(80 s)/Ti electrode. As expected, the CD was observed to increase with increasing concentration (Fig. 2a). In the GC profiles and the production amounts (Fig. 2b, c, Fig. S8, and Table S8), CH₄, C₂H₄ and C₂H₆ were substantially increased in 0.5 M condition. The FE (and the amount) of H₂ increased with increasing the concentration, while the FE (and the amount) of CO decreased with concentration (Fig. 2d). Consequently, the CO/H₂ ratio was observed to decrease with potential (Fig. S8). For C_{3–7} hydrocarbons (Figs. 1e, f, and S8), the amounts (ppm) and FEs were dramatically increased in the 0.5 M condition. These results indicate that when available H⁺/H* species are more abundant, greater amounts of hydrocarbons are produced, as previously mentioned. For the C_nH_{2n+2}/C_nH_{2n} ratios over Au(80 s)/Ti (Fig. S8), the ratios were estimated to be between 2 and 4, indicating that alkanes were produced more than the corresponding alkenes.

To understand the production of long-chain hydrocarbons, we plotted the Anderson-Schulz-Flory (ASF) equation of $\ln(w_n/n) = n \ln \alpha + b$ constant with respect to carbon number (n), mass fraction of a hydrocarbon product (w_n), and hydrocarbon chain growth probability (α) [40,47]. The plots of C_nH_{2n} and C_nH_{2n+2} showed very good linearity, and their α values were determined to be 0.445 and 0.336, respectively. These results suggest that long-chain hydrocarbons were produced by consecutive C–C coupling polymerization, as observed in the conventional F-T synthesis, which will be discussed further below.

To further investigate the effect of concentration, we tested a low-coverage Au(10 s)/Ti electrode in various concentrations of KHCO₃ electrolyte (Fig. 3 and Table S9). The amperometry i-t curves are presented in Fig. 3a, and it was found that the CDs were fairly stable at low concentrations, but the CD at 0.5 M changed substantially with time. This suggests that the electrode was more affected by the concentration. As shown in Fig. 3b, b1, and Fig. S9, H₂, CH₄, C₂H₄, and C₂H₆ production increased with increasing concentration. The production of C_{3–7} hydrocarbons was maximized at the highest concentration of 0.5 M (Figs. 3c and S8), and the C_nH_{2n+2}/C_nH_{2n} ratios indicated that alkanes were produced more than corresponding alkenes (Fig. S8). The FE of H₂ was somewhat less at 0.2 M compared to other conditions (Fig. 3d), and the FE of CO was dramatically decreased with increasing concentration (Fig. 3e), suggesting that CO₂ adsorption was affected by H or surface CO was hydrogenated to form hydrocarbons. As expected, the FEs of CH₄ and C_{2–5} hydrocarbons increased at higher concentrations (Fig. 3f). In Figs. 2f and 3f, the Au(10 s)/Ti electrode exhibited better performance in the production of CH₄ and C_{2–5} hydrocarbons under 0.1 M and 0.2 M conditions, compared to the Au(80 s)/Ti electrode. However, at a higher concentration of 0.5 M, the Au(80 s)/Ti electrode produced more hydrocarbons. These results highlight the significance of both Au thickness and electrolyte concentration in hydrocarbon production.

3.3. Concentration effects on EC CO reduction over Au(10 s)/Ti in CO-saturated KHCO₃ electrolyte

As discussed above, the production of C_{3–5} hydrocarbons at $-1.6 \text{ V}_{\text{Ag/AgCl}}$ in CO₂-saturated 0.1 M KHCO₃ was found to be maximized over the Au(10 s)/Ti electrode. Therefore, the Au(10 s)/Ti

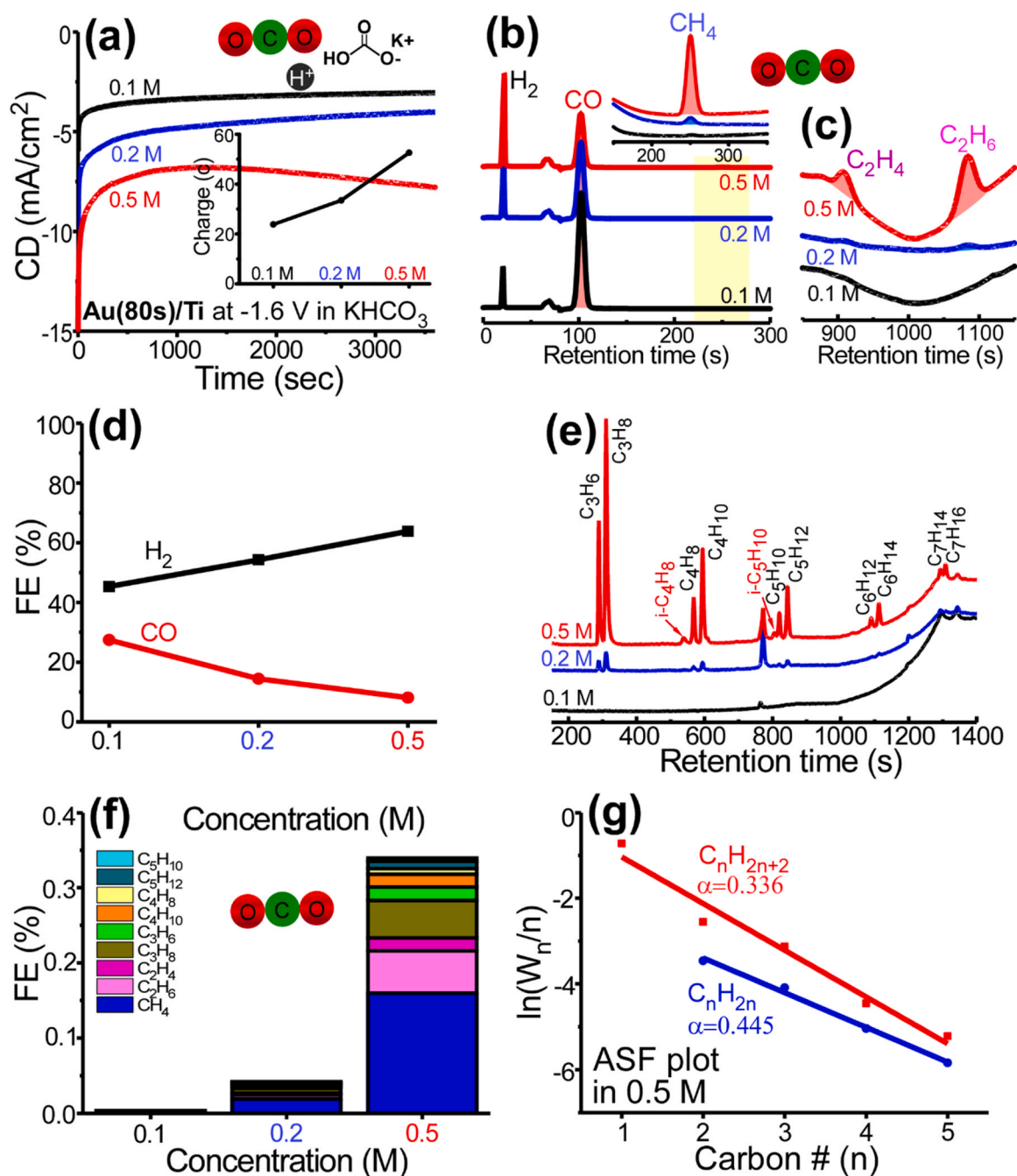


Fig. 2. Amperometry i-t curves (corresponding charges in the inset) over Au(80 s)/Ti electrode at $-1.6 \text{ V}_{\text{Ag}/\text{AgCl}}$ in CO₂-saturated 0.1 M, 0.2 M, and 0.5 M KHCO₃ electrolytes (a). GC profiles for H₂, CO, and CH₄ products (b). GC profiles for C₂H₄ and C₂H₆ products (c). FEs of CO and H₂ products (d). GC profiles separated by HP-Plot Q PT column (e). FEs of CH₄ and C₂₋₅ compounds (f). ASF distribution plots for the hydrocarbon products (g).

electrode with low Au coverage was selected to examine CO-saturated conditions. The aim of this experiment was to demonstrate the production of hydrocarbons using directly adsorbed CO. The CD behavior with concentration was observed to be similar to that of the Au(10 s)/Ti electrode in CO₂-saturated conditions (Fig. 4a). The CD (or total charge) increased with increasing concentration.

The FE of H₂ and its production amount increased with increasing concentration (Fig. S10 and Table S10). As shown in Fig. 4b and Table S10, the C₃₋₇ hydrocarbons were substantially increased in higher concentrations, similar to the results for the Au(10 s)/Ti and Au(80 s)/Ti electrodes discussed above. The C_nH_{2n+2}/C_nH_{2n} ratios of between 1.5 and 3 indicated that alkanes were produced more than the corresponding alkenes (inset of Fig. 4b). The total FE of CH₄ and C₂₋₅

hydrocarbons was maximized in 0.2 M conditions (Fig. 4c). Their production amounts increased with increasing concentration (Fig. 4d and e) due to an increase in CD. The observed FEs of CH₄ and C₂₋₅ hydrocarbons in CO₂ and CO-saturated conditions were analyzed using (FE_{CO} - FE_{CO2})/FE_{CO2} ratios in Fig. 4f. The positive values indicated that the FE in CO conditions was larger. It was interesting to note that CH₄ production commonly decreased when CO₂ was replaced by CO. On the other hand, the FEs of C₂₋₅ hydrocarbons all increased in CO-saturated conditions. This indicated that directly adsorbed CO efficiently participated in the hydrogenation reaction with surface H* to produce hydrocarbons. This also indicates that the direct adsorption of CO was enhanced on the surface of the Au(10 s)/Ti electrode, resulting in increased CO hydrogenation.

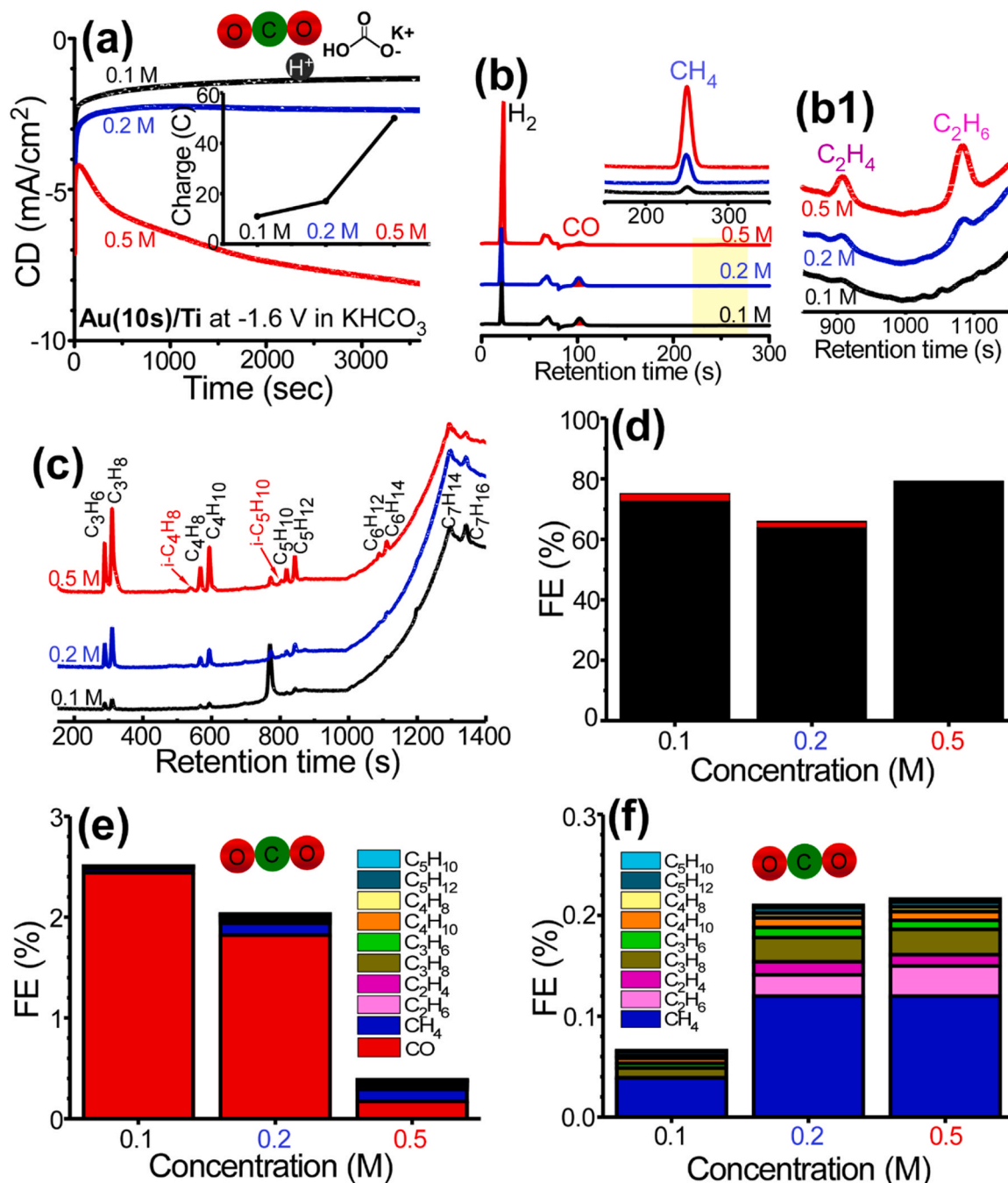


Fig. 3. Amperometry i-t curves (corresponding charges in the inset) at -1.6 V_{Ag/AgCl} over Au(10 s)/Ti electrode in CO₂-saturated 0.1 M, 0.2 M, and 0.5 M KHCO₃ electrolytes (a). GC profiles for H₂, CO, and CH₄ products (b). GC profiles for C₂H₄ and C₂H₆ products (b1). GC profiles separated by HP-Plot Q PT column (c). FEs of CO and H₂ products (d). FEs of CO, CH₄, and C₂₋₅ compounds (e). FEs of CH₄ and C₂₋₅ compounds (f).

3.4. EC CO₂ reduction tests over Au/Ti in CO₂-saturated 0.1 M K₂HPO₄/KH₂PO₄ buffer electrolyte

The performance of CO₂ reduction was further demonstrated using an additional electrolyte of 0.1 M 0.1 M K₂HPO₄/KH₂PO₄ buffer.

3.4.1. Au thickness effects

The EC CO₂ reduction experiment was conducted on an Au/Ti electrode with varying Au deposition times at an applied potential of -1.6 V_{Ag/AgCl} in the electrolyte. The amperometry i-t curves in Fig. 5a demonstrate that the current density (CD) was dependent on the thickness of the Au overlayer within the range of 5–20 mA/cm². As

previously mentioned, the deposition times of 10 s, 20 s, 80 s, 160 s, and 640 s correspond to calibrated thicknesses of 0.5 nm, 1.0 nm, 3.8 nm, 7.7 nm, and 30.7 nm, respectively. In the GC profiles for H₂, CO, CH₄, and C₂₋₇ hydrocarbons (Fig. S11), the production amounts of these gases were dependent on the thickness of the Au overlayer (as shown in Fig. S11 and Table S11). Specifically, the FE of H₂ was gradually decreased with increasing Au deposition time and minimized the Au (160 s)/Ti electrode (Fig. 5b), while the FEs of CO and other gases (CO, CH₄, and C₂₋₅ hydrocarbons) were maximized over the Au(640 s)/Ti electrode (Fig. 5c and d). The CO/H₂ ratio was therefore maximized over the Au(640 s)/Ti electrode (inset of Fig. 5b). The FE of CO over the Au (640 s)/Ti electrode was observed to be higher than that over the bare

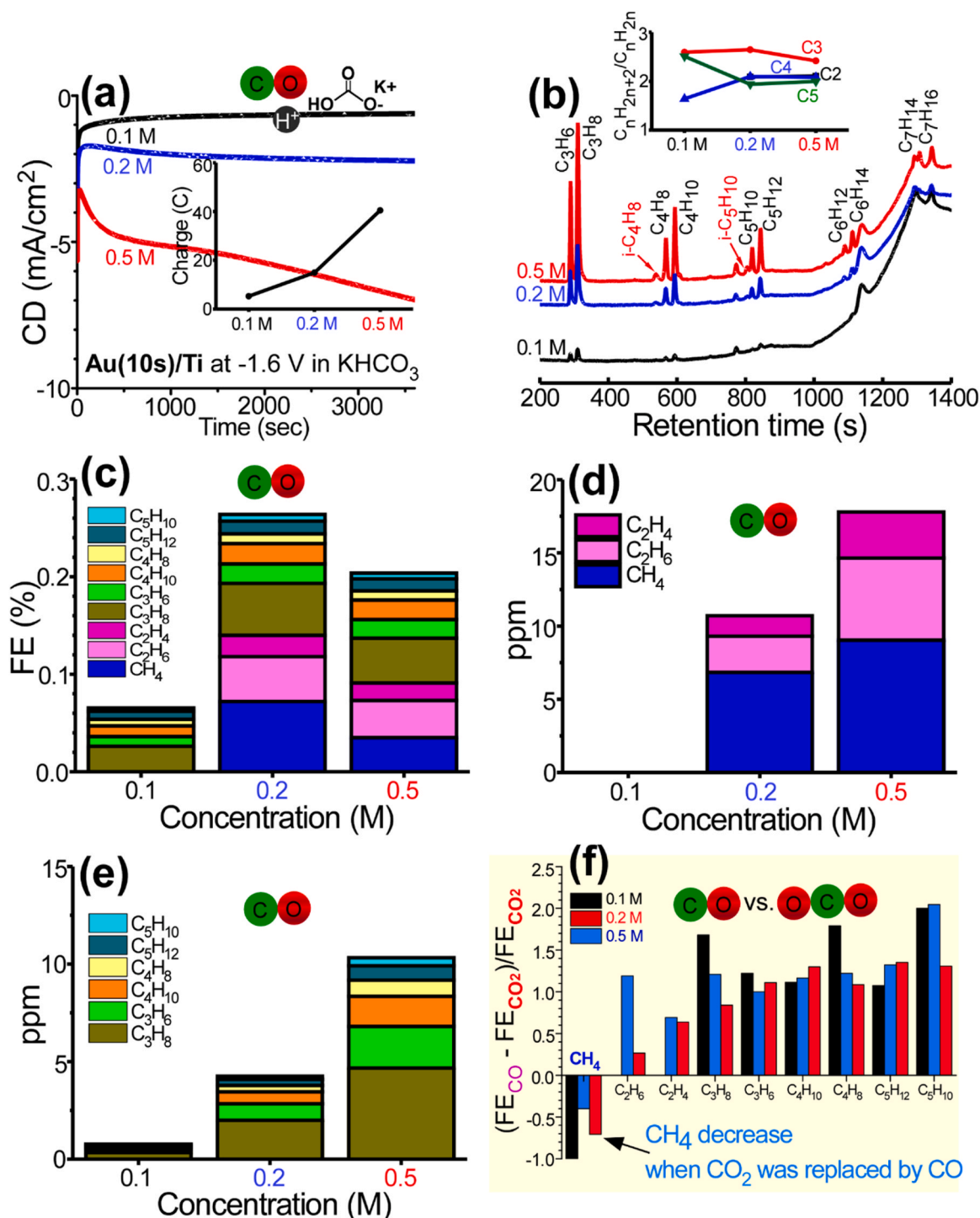


Fig. 4. Amperometry i-t curves (corresponding charges in the inset) at -1.6 V_{Ag/AgCl} over Au(10 s)/Ti electrode in CO-saturated 0.1 M, 0.2 M, and 0.5 M KHCO₃ electrolytes (a). GC profiles separated by HP-Plot Q PT column and the corresponding C_nH_{2n+2}/C_nH_{2n} ratios in the inset (b). FEs of CH₄ and C₂₋₅ compounds (c). CH₄, C₂H₄, and C₂H₆ product amounts (d). Amounts of C₃₋₅ compounds (e). $(FE_{CO} - FE_{CO_2}) / FE_{CO_2}$ ratios, where FE_{CO} and FE_{CO₂} (in Fig. 3) are FEs measured in CO and CO₂-saturated electrolyte conditions, respectively (f).

Au electrode, but the FE of H₂ was higher than that over bare Au (Fig. 5b). The FEs of CH₄ and C₂₋₇ hydrocarbons over the bare Au electrode were somewhat lower than those over the Au(640 s)/Ti electrode (Fig. 5d), indicating that the Au/Ti interface plays a significant role in CO₂ reduction.

The C_nH_{2n+2}/C_nH_{2n} ratios (Fig. 5e) were observed to be between 1.5 and 3 and increased with increasing Au deposition time, indicating that alkanes were produced more when the Au layer became thicker. For the

ASF plots (Fig. 5f), the α values for C_nH_{2n} and C_nH_{2n+2} were found to be 0.440 and 0.327, respectively. The plots show good linearity, suggesting that consecutive C-C coupling polymerization reactions are occurring.

3.4.2. Applied potential effects over Au(80 s)/Ti electrode

The Au(80 s)/Ti electrode was selected and tested at various applied potentials (Fig. 5g, h, Fig. S12, and Table S12). As expected, the CD (and total change) increased with increasing applied potential (Fig. S12). In

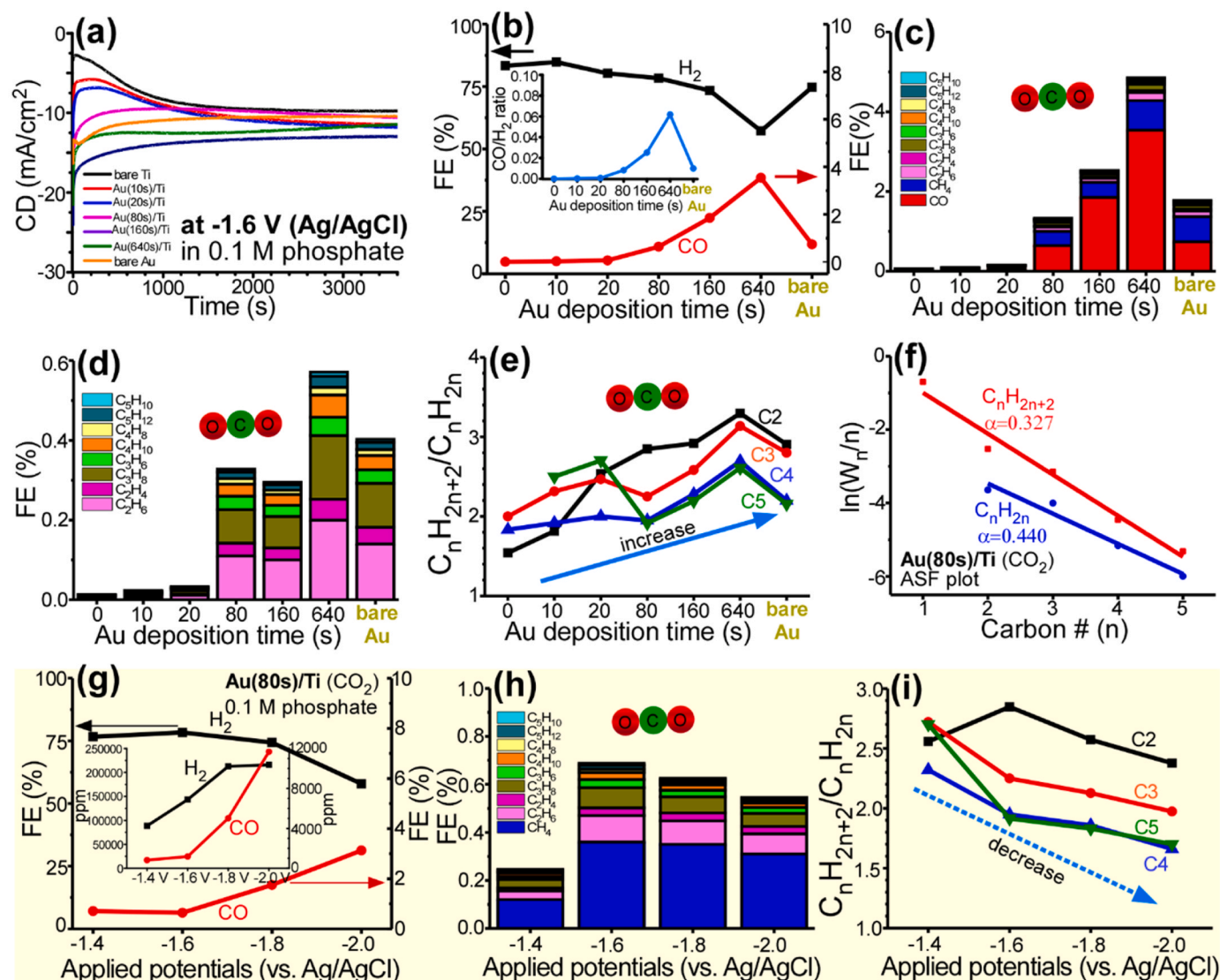


Fig. 5. Amperometry *i-t* curves for bare Ti, Au/Ti with Au deposition time, and bare Au electrodes at $-1.6 \text{ V}_{\text{Ag/AgCl}}$ (a). FEs of CO and H_2 , and the CO/H_2 ratio in the inset (b). FEs of CO, CH_4 , and C_{2-5} compounds (c). FEs of C_{2-5} compounds (d). $\text{C}_n\text{H}_{2n+2}/\text{C}_n\text{H}_{2n}$ ratios of C_{2-5} products (e). ASF distribution plots for the hydrocarbon products (f). FEs of CO and H_2 products over Au(80 s)/Ti at -1.4 V , -1.6 V , -1.8 V , and $-2.0 \text{ V}_{\text{Ag/AgCl}}$ in $0.1 \text{ M K}_2\text{HPO}_4/\text{KH}_2\text{PO}_4$ buffer for 1 h (g), and the CO and H_2 production amounts in the inset. FEs of CH_4 and C_{2-5} compounds (h). Corresponding $\text{C}_n\text{H}_{2n+2}/\text{C}_n\text{H}_{2n}$ ratios for C_{2-5} compounds (i).

the GC profiles, the production amounts (ppm) of H_2 , CO, CH_4 , and C_{2-7} hydrocarbons increased with increasing potential, due to an increase in total charge (Fig. S12). The FE of H_2 gradually decreased and that of CO increased with increasing the applied potential. The FEs of H_2 and CO were observed to be 57.9% and 3.1% at $-2.0 \text{ V}_{\text{Ag/AgCl}}$, respectively. For the FEs of CH_4 and C_{2-7} hydrocarbons (Fig. 5h), the FEs were maximized at $-1.6 \text{ V}_{\text{Ag/AgCl}}$. The $\text{C}_n\text{H}_{2n+2}/\text{C}_n\text{H}_{2n}$ ratios were observed to be between 1.5 and 3 and inversely decreased with increasing potential (Fig. 5i). This reflects that alkanes were produced more than the corresponding alkenes. Recycling was tested over the Au(80 s)/Ti electrode (Fig. S13 and Table S13). Plausibly due to deterioration of the Au/Ti interfacial activity, H_2 , CO, CH_4 , and C_{2-7} hydrocarbons were observed to all decrease with increasing cycling number.

3.5. EC CO reduction over Au/Ti in CO-saturated $0.1 \text{ M K}_2\text{HPO}_4/\text{KH}_2\text{PO}_4$ buffer electrolyte

CO-saturated conditions were also tested for the Au/Ti electrode with different Au deposition times at an applied potential of $-1.6 \text{ V}_{\text{Ag/AgCl}}$. Surface CO and H are directly formed, as depicted in Fig. 6a. The

measured CD ($1\text{--}10 \text{ mA}/\text{cm}^2$) for each electrode is shown in the amperometry *i-t* curves (Fig. 6a1). The CD for the bare Au electrode was lower than that of other electrodes. CH_4 and C_{2-7} hydrocarbons showed high production in the Au deposition range of 80–640 s (Figs. 6b, c, and S14). In this range, their production amounts and FEs were much higher than those observed with the bare Au electrode. Unlike the bare Au electrode in CO_2 -saturated conditions (Fig. 5c, d, and h above), C_2H_4 and C_2H_6 were significantly reduced in CO-saturated conditions (Fig. 6b, c, and Table S14). The FEs of CH_4 and C_{2-7} hydrocarbons over Au/Ti electrodes in CO-saturated conditions were comparable to those in CO_2 -saturated conditions. H_2 production amounts were also observed to be higher in the Au deposition ranges of 80–640 s (Fig. S14). For the $\text{C}_n\text{H}_{2n+2}/\text{C}_n\text{H}_{2n}$ ratios (Fig. 6d), the ratios were observed to be between 1.5 and 3 and increased with increasing Au deposition time, the same as in CO_2 -saturated conditions (Fig. 5e above). The ASF plots for Au(80 s)/Ti (Fig. 6e) gave α values of 0.437 and 0.351 C_nH_{2n} and $\text{C}_n\text{H}_{2n+2}$, respectively. The linearity and slope were similar to the plots in CO_2 -saturated conditions.

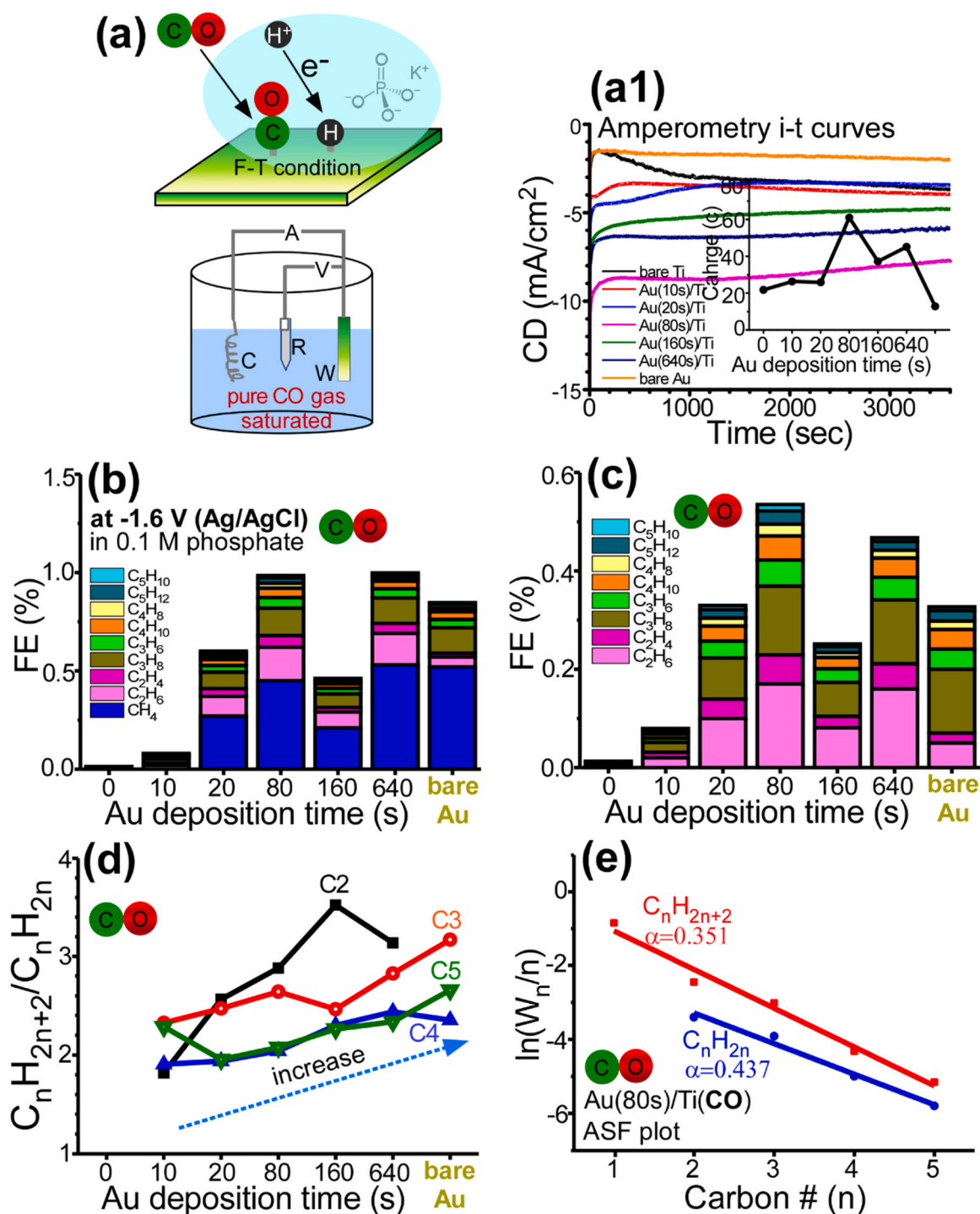


Fig. 6. Scheme for EC CO reduction in CO-saturated in 0.1 M K₂HPO₄/KH₂PO₄ buffer (a). Amperometry i-t curves (corresponding charges in the inset) at -1.6 V_{Ag/AgCl} over bare Ti and Au/Ti electrodes (a1). FEs of CH₄ and C₂₋₅ compounds (b). FEs of C₂₋₅ compounds (c). C_nH_{2n+2}/C_nH_{2n} ratios for C₂₋₅ compounds (d). ASF distribution plots for the hydrocarbon products (e).

3.6. Surface morphology, interfacial electronic structures, and electrochemical active areas

XRD, SEM, EDXS, UPS, and XPS techniques were utilized to investigate the crystalline state, surface morphology, density of states (DOS) near the Fermi level, and surface oxide states of the samples.

3.6.1. XRD, SEM, and EDXS data

The XRD patterns of the bare Ti and Au(640 s)/Ti electrodes were

similar, with the XRD signals mainly attributed to metallic Ti (Fig. 7a). Weak signals of metallic Au XRD were seen around $2\theta = 38^\circ$, attributed to the (111) plane of cubic phase metallic Au [48]. EDXS was used to examine the uniform distribution of Au on Ti support (Fig. 7b). A Au (160 s)/Ti electrode was chosen for sufficient EDX signal. The SEM image revealed even distribution of Au film on the support, despite the presence of grain boundaries. The EDX spectrum showed dominant Ti and Au signals, with a weak oxygen signal. The EDX Au/Ti atomic ratio for Au(160 s)/Ti was estimated as 0.6/100. Elemental mapping images

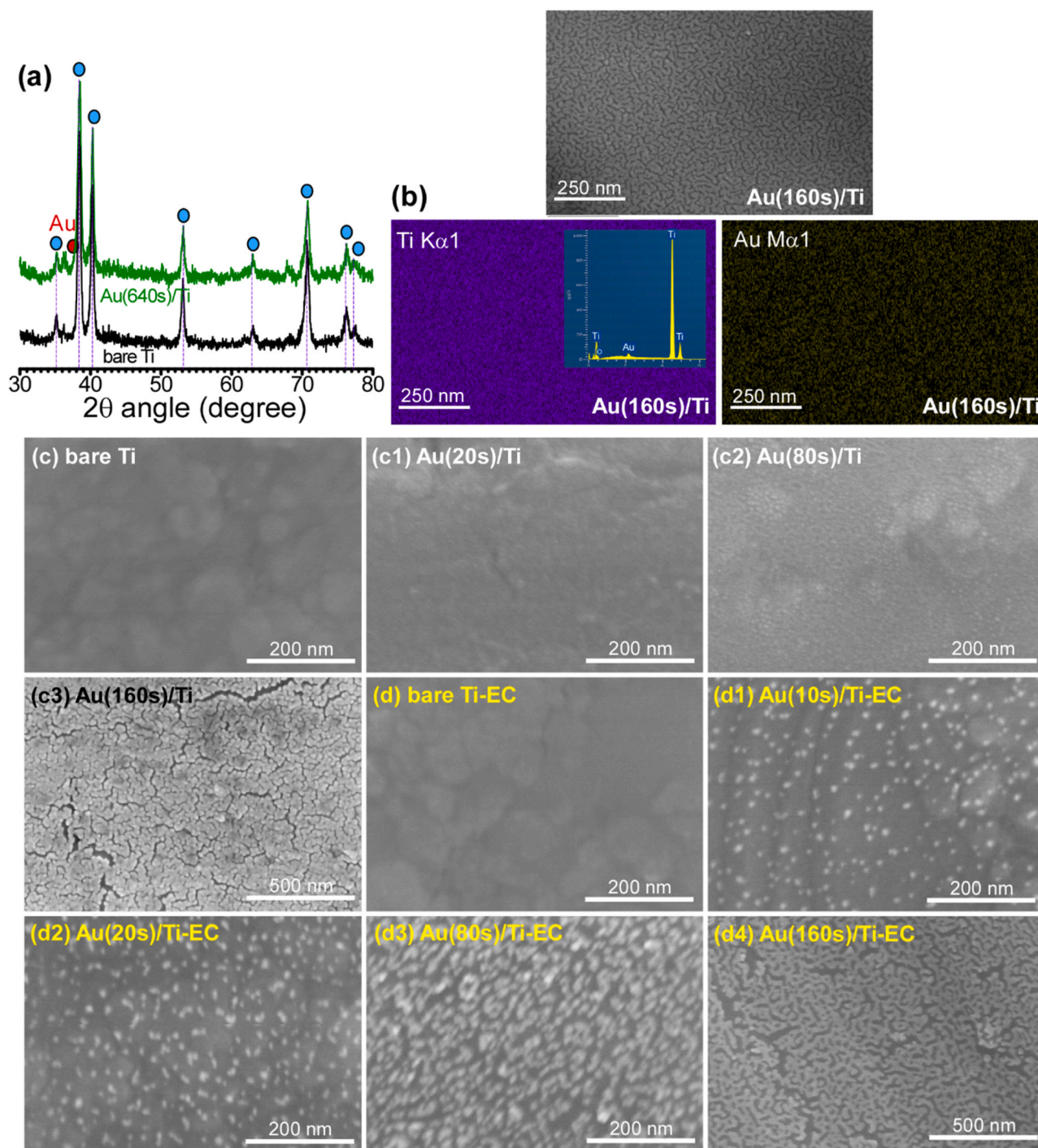


Fig. 7. XRD profiles of selected bare Ti and Au(640 s)/Ti electrodes (a). EDX SEM and elemental mapping images of Ti and Au, and EDX spectrum in the inset (b). SEM images of as-prepared bare Ti and Au/Ti (20 s, 80 s, and 160 s) electrodes (c, c1, c2, and c3). SEM images of bare Ti and Au/Ti (10 s, 20 s, 80 s, and 160 s) electrodes after EC tests (d, d1, d2, d3, and d4).

confirmed the even distribution of Au on the surface of the as-prepared electrode.

SEM images were taken for bare Ti and Au/Ti electrodes before and after EC tests (Fig. 7c-c3 and d-d4). The SEM images of Au/Ti electrodes showed significant differences compared to bare Ti before EC experiments. In the case of Au(20 s)/Ti, the Au image was barely distinguishable from Ti (Fig. 7c1), whereas the overlaid Au layer in Au(80 s)/Ti was clearly visible (Fig. 7c2). It was evident that Au was uniformly distributed on the Ti support. The SEM image of Au(160 s)/Ti (Fig. 7c3) further confirmed the even distribution of Au, as discussed in Fig. 7b.

After EC experiments, the SEM images showed no significant change in bare Ti before and after (Fig. 7d). However, in the SEM images of Au/Ti electrodes with low deposition times of 10 s, 20 s, and 80 s (Fig. 7d1, d2, and d3), the overlaid Au formed clustered larger nanoparticles or islands. The density of Au particles increased with longer deposition times, as expected. In the SEM image of the Au(160 s)/Ti electrode (Fig. 7d4), the Au grains appeared more contracted, revealing more open areas. Nonetheless, the overlayer Au remained evenly distributed on the surface after EC. The increased open areas may suggest an expanded Au/Ti interface, which likely contributes to the process of EC

CO₂/CO reduction.

3.6.2. XPS and UPS data

XPS data were obtained for the Au/Ti electrode with different Au deposition times (Fig. 8a, a1, a2, and a3). For the Ti 2p XPS profiles, a Ti 2p_{3/2} peak was observed at a binding energy (BE) of 454.1 eV, attributed to metallic Ti⁰. Two strong Ti 2p_{3/2} and Ti 2p_{1/2} peaks were observed at 458.7 eV and 464.3 eV, attributed to Ti⁴⁺ oxides [49–51]. The Ti 2p peaks diminished with increasing Au deposition time and almost disappeared upon Au deposition for 640 s. In Fig. 8a1, two O 1s XPS peaks were assigned at 530.2 eV and 531.8 eV, attributed to lattice (O²⁻ of

TiO₂) and surface (OH/H₂O) oxides, respectively. The lattice oxide peak at 530.2 eV was dominant for bare Ti but became diminished with increasing overlayer Au. For the Au(640 s)/Ti electrode, the O 1s peak was quite suppressed, and the surface oxide peak became larger than the lattice oxide peak. The Au 4f peaks increased with increasing Au deposition time, as expected (Fig. 8a2). The Au 4f_{7/2} and Au 4f_{5/2} XPS peaks were observed at 84.0 eV and 87.7 eV, respectively, and slightly shifted to 83.8 eV and 87.5 eV, respectively, upon Au deposition for 640 s [46,48]. The valence band structure substantially increased with increasing Au deposition (Fig. 8a3). Au 5d bands were clearly observed upon Au deposition for 20 s

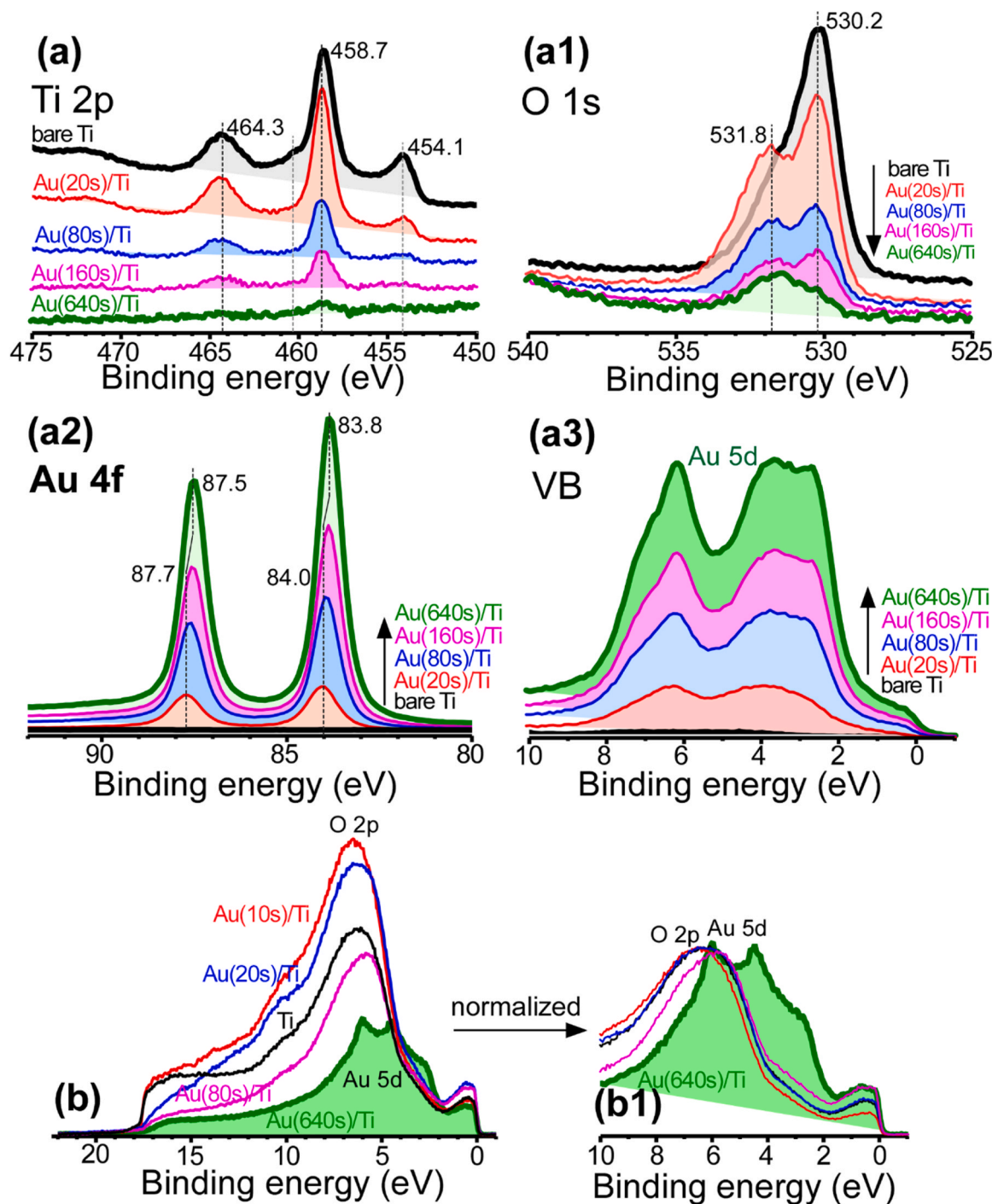


Fig. 8. Ti 2p, O 1s, Au 4f, and VB XPS profiles for bare Ti and Au/Ti with Au thickness (a, a1, a2, and a3, respectively). UPS profiles (b) and the normalized spectra (b1) for bare Ti and Au/Ti with Au thickness.

The thickness of the Au overlayer was examined using XPS data. The Au(20 s)/Ti electrode was chosen because its thickness was smaller than the electron mean free path (1.78 nm) of the Au overlayer signal [52]. The XPS thickogram was used to determine the overlayer thickness, as described in detail in the literature [53]. The calculation involved the XPS areas of Ti 2p and Au 4f signals, relative XPS sensitivity factors (6.25 for Au 4f and 2.0 for Ti 2p) [54], kinetic energies of Ti 2p and Au 4f signals, and XPS takeoff angle (90 degrees). The estimated overlayer Au thickness for Au(20 s) was 1.1 nm, in good agreement with the thickness of 1.0 nm, mentioned in the experimental section.

UPS data were obtained for Au/Ti with different Au deposition times (Fig. 8b and b1), showing that the work function somewhat increased upon Au deposition. The work functions of bare Ti and Au(640 s)/Ti electrodes were measured to be 3.2 eV and 3.4 eV, respectively. The density of states (DOS) near the Fermi level was observed to be high, indicating a possibility of high surface H^* [34,35]. In the normalized spectra (Fig. 8b1), the Au 5d bands were clearly observed around 6 eV and 4 eV for the Au(640 s)/Ti electrode, but not in the UPS for the Au (20 s)/Ti [48].

In Fig. 9, for the selected Au(80 s)/Ti electrode after EC tests at various applied potentials of -1.4 V, -1.6 V, and -2.0 V_{Ag/AgCl}, the Ti 2p peak positions showed no change before and after EC tests (Fig. 9a). However, the Ti 2p intensity increased somewhat after EC tests due to a change in the morphology of the overlayer Au. This also indicates that the Ti support became exposed. The corresponding O 1s peak (and the lattice oxide peak) in Fig. 9b increased after EC tests, reflecting that the

Ti support was exposed. For the Au 4f and VB XPS peaks (Fig. 9c and d), the intensities somewhat decreased after EC tests, due to a change in morphology from films to grains, as shown in Fig. 7.

In the next section, we will discuss the reduction mechanism, but it's worth noting here that we didn't detect a Pt 4f XPS signal in the XPS spectra. This suggests that there was no dissolution of the Pt counter electrode and subsequent deposition onto the Au/Ti working electrode. As a result, the electrode's performance can be attributed primarily to the Au and Ti components.

3.6.3. Electrochemical active surface area (ECSA)

To assess the significance of the Au/Ti interface, ECSA measurements were briefly introduced following the Experimental section [55,56]. Among various experimental parameters in electrochemistry, ECSA serves as a useful parameter for controlling the electrode's EC reduction efficiency. ECSA is calculated using the formula $ECSA = C_{dl}/C_s$, where C_{dl} represents the electrochemical double layer capacitance and C_s denotes the specific capacitance of the electrode (assumed to be $40 \mu\text{F}/\text{cm}^2$ for simplicity in this study) [55,56]. C_{dl} is estimated from the CV curves obtained at different scan rates (Fig. S15), plotting the values of $(i_a - i_c)/2$ against the scan rates, where i_a and i_c refer to the anodic and cathodic currents, respectively. By determining the 1/2 slope, the C_{dl} value for each electrode was obtained: $32.9 \mu\text{F}/\text{cm}^2$ for bare Ti, $73.8 \mu\text{F}/\text{cm}^2$ for Au(160 s)/Ti, and $3.23 \mu\text{F}/\text{cm}^2$ for bare Au. Consequently, the ECSA value was consistently observed to be higher for Au/Ti electrodes compared to bare Ti and bare Au electrodes (Fig. S15): for example,

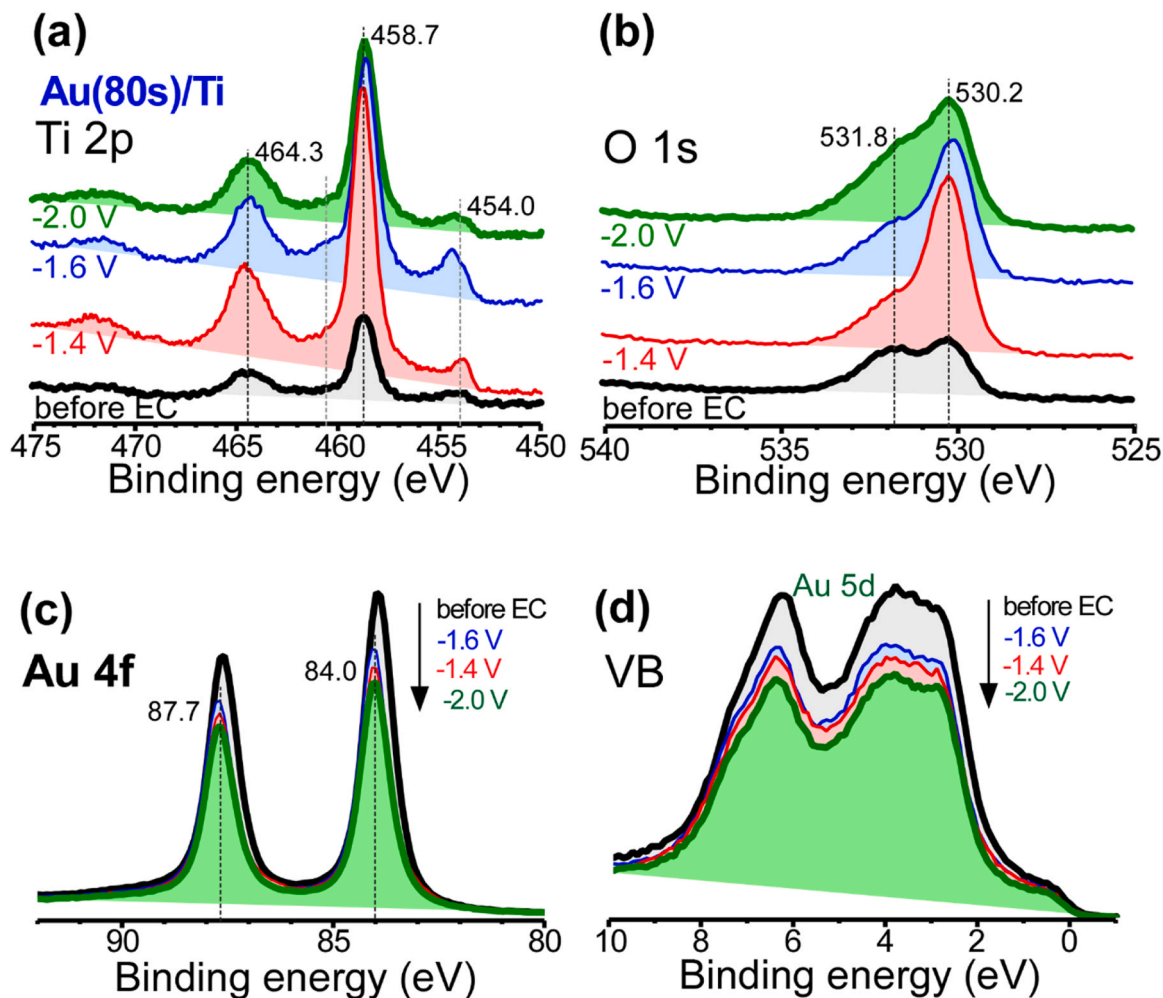


Fig. 9. Ti 2p, O 1s, Au 4f, and VB XPS profiles (a, b, c, and d, respectively) for Au(80 s)/Ti electrode before and after amperometry tests at -1.4 V, -1.6 V, -1.8 V, and -2.0 V_{Ag/AgCl}.

0.82/cm² for bare Ti, 1.85/cm² for Au(160 s)/Ti, and 0.08/cm² for bare Au. This suggests an increase in active sites at the interface of Au and Ti.

3.7. EC CO₂ reduction and CO reduction mechanism via initial CO₂ and CO adsorption paths

The electrochemical demonstration experiments were conducted under CO₂- and CO-saturated conditions in an aqueous (H⁺/H₂O) electrolyte. The experimental setup involved the initial adsorption of CO₂ followed by direct CO adsorption to achieve surface CO (Fig. 10). Surface H was formed via the reaction $H^+ + e^- \rightarrow H^*$, and both surface *CO and H* were produced on the catalyst surface, as in the conventional F-T synthesis. The electrochemical combination of CO and H led to hydrocarbon generation. The electrochemical process involved plausible mechanisms such as Langmuir-Hinshelwood and Eley-Rideal [57,58]. To achieve high-efficiency F-T synthesis, strong adsorption of both surface CO and H is crucial. As mentioned earlier in the Introduction, Au is recognized for its high CO production in EC CO₂R [29–32], while Ti is known for its significant surface H production [33–35]. Thus, Au promotes surface CO, and Ti promotes surface H, both of which contribute to hydrocarbon production in the F-T synthesis process.

In both conditions, surface H was predominantly formed and released as H₂ via $H^* + H^* \rightarrow H_2$ (Langmuir-Hinshelwood mechanism)

and $H^* + H^+ + e^- \rightarrow H_2$ (Eley-Rideal mechanism) [10,34,35]. In CO₂-saturated conditions, CO₂ was adsorbed via $CO_2 + H^+ + e^- \rightarrow HOOC^*$, where C* indicates C bonded with the metal surface (M), M–C, as shown in Fig. 10. The intermediate OCHO species with M–O bond were plausibly formed and transformed into formate [59–61]. However, formate formation was negligible in this study. HOOC* species is known to convert to surface CO species via $HOOC^* + H^+ + e^- \rightarrow ^*CO + H_2O$ [11–15,31–33]. The CO is either released as gaseous CO or combined with H* for hydrogenation reactions.

In CO-saturated conditions, CO is expected to be directly adsorbed on active sites with proper binding strength for hydrogenation. The active sites (or CO bonding strength with catalyst surface) may influence the performance of hydrogenation reactions. As observed above, bare Au and Ti showed poorer hydrocarbon production compared to Au/Ti electrodes in CO-saturated conditions. This indicates that CO is poorly adsorbed on bare Au and Ti [62]. However, the interface of Au and Ti showed enhanced CO adsorption.

Now, both indirectly formed CO and directly adsorbed CO are expected to combine similarly with surface *H. The good linearity of the ASF plots in both CO₂ and CO-saturated conditions [47,63,64] indicates that their hydrocarbon productions are similar to those in conventional F-T synthesis. *COH is an initial intermediate formed through the reaction of CO and H, where H* represents either M–H or H⁺ + e[−]; one for

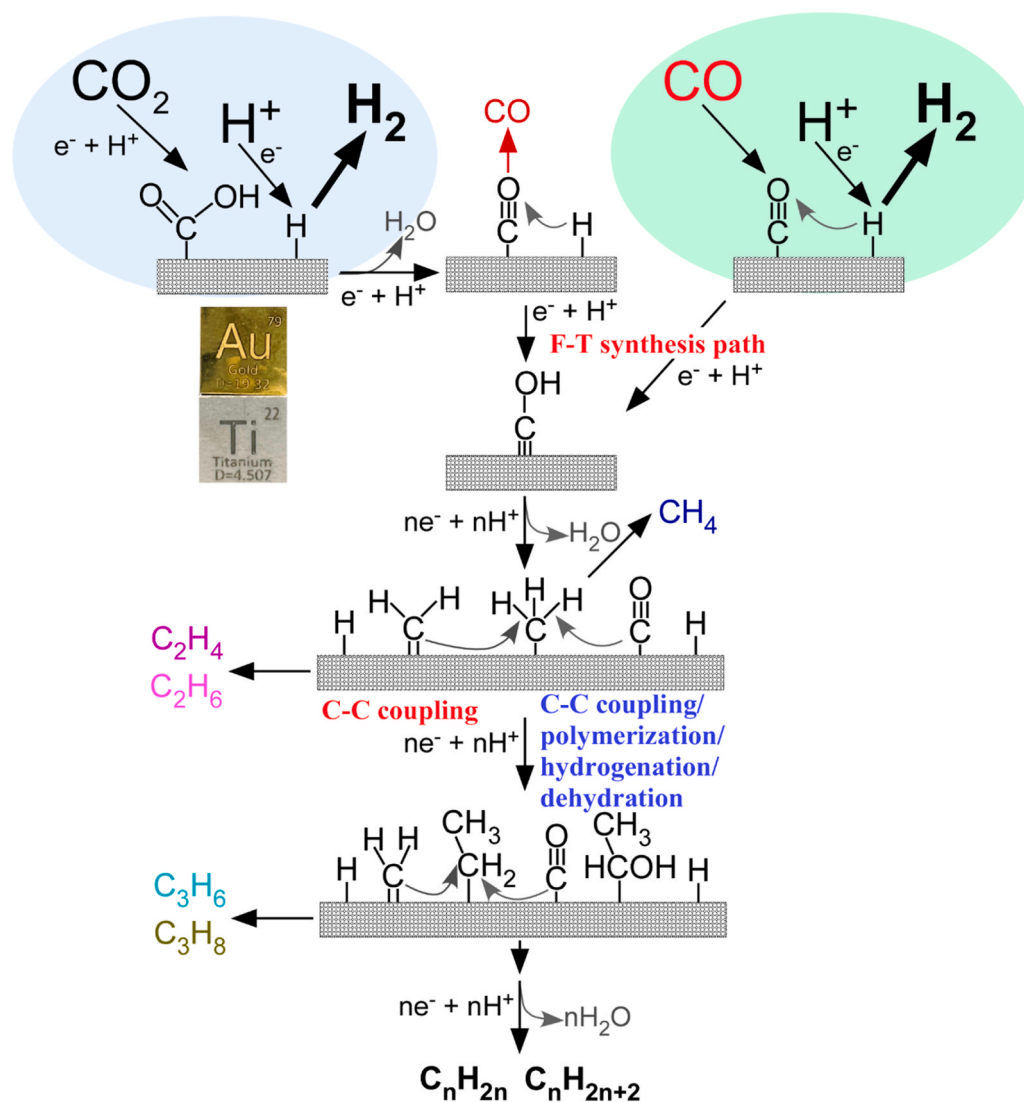


Fig. 10. Initial adsorptions of CO₂, CO, and H⁺ on electrode surface, and the hydrocarbon production F-T synthesis mechanism.

the Langmuir-Hinshelwood mechanism and the other for the Eley-Rideal mechanism, both of which are involved in hydrocarbon production [57, 58].

The hydrogenation processes include $\text{CO} + 4\text{H} \rightarrow \text{*CH}_2 + \text{H}_2\text{O}$ and $\text{CO} + 5\text{H} \rightarrow \text{*CH}_3 + \text{H}_2\text{O}$. CH_4 is then released via association of *CH_x and H^* . To produce C_{2-7} hydrocarbons, a C–C coupling mechanism is included, between *CH_x species or between *CO and *CH_x intermediates [36,37,63,64]. The $\text{*CO} - \text{*CO}$ coupling mechanism is also a plausible mechanism for C_{2+} products [11–15]. However, oxygenated hydrocarbons such as ethanol, acetate, and propanol were not detected, and therefore this coupling process was excluded in the present study. The association between *CH_x species produces gaseous C_2H_4 and C_2H_6 . Otherwise, $\text{*CH}_2\text{CH}_3$ species are retained on the surface to generate longer chains. The association between *CO and *CH_x may include $\text{*CO} + \text{*CH}_3 + \text{H}^* \rightarrow \text{*CH(OH)CH}_3$, followed by dehydration forming $\text{*CH}_2\text{CH}_3$. For C_3 hydrocarbons, two plausible mechanisms include 1) $\text{*CH}_2\text{CH}_3 + \text{*CH}_x + \text{nH}^* \rightarrow \text{C}_3\text{H}_6$ or C_3H_8 , and 2) $\text{*CH}_2\text{CH}_3 + \text{*CO} + \text{nH}^* \rightarrow \text{*CH(OH)CH}_2\text{CH}_3$, followed by dehydration forming C_3H_6 or C_3H_8 . If C_3 hydrocarbons are not released, $\text{*CH}_2\text{CH}_2\text{CH}_3$ species are retained on the surface to generate longer chains. Consequently, C–C coupling, polymerization, hydrogenation, and dehydration processes produce $\text{C}_n\text{H}_{2n+2}$ and C_nH_{2n} . All these processes are highly related to the CO and H_2 ratio, as discussed above. The association between longer chains is expected to be much slower due to steric and kinetic factors. Instead, surface *CH_x and *CO are more easily generated on neighboring sites to participate in C–C coupling by insertion mechanism, as depicted in Fig. 10. In CO-saturated condition, gaseous CO can also be associated with surface hydrocarbon species via Eley-Rideal mechanism to produce longer chains. For example, it includes $\text{*CH}_2\text{CH}_3 + \text{CO (g)} + \text{nH}^* \rightarrow \text{*CH(OH)CH}_2\text{CH}_3$. Overall, the electrochemical reactions in CO-saturated condition are $2(2n+1)\text{H}^+/\text{e}^- + \text{nCO} \rightarrow \text{C}_n\text{H}_{2n+2} + \text{nH}_2\text{O}$ and $4n\text{H}^+/\text{e}^- + \text{nCO} \rightarrow \text{C}_n\text{H}_{2n} + \text{nH}_2\text{O}$ for alkanes and alkenes, respectively.

In CO_2 -saturated condition, the overall reactions are $(3n+1)\text{H}^+/\text{e}^- + \text{nCO}_2 \rightarrow \text{C}_n\text{H}_{2n+2} + 2n\text{H}_2\text{O}$ and $6n\text{H}^+/\text{e}^- + \text{nCO}_2 \rightarrow \text{C}_n\text{H}_{2n} + 2n\text{H}_2\text{O}$ for alkanes and alkenes, respectively. Zhou et al. proposed a coupling between *COOH and *CH_x for the C–C coupling reaction in CO_2 -saturated electrolyte, followed by CH_x insertion for the production of longer hydrocarbons [65]. However, it should be noted that *COOH cannot be formed in CO-saturated conditions. Therefore, an alternative reaction mechanism must also be involved in the production of long-chain hydrocarbons. As a result, we introduce the conventional F–T synthesis mechanism based on the ASF plots to provide a more comprehensive understanding of the process. A based on experimental results, the Au/Ti interface is believed to be crucial for adsorption, formation of neighboring *CO and *H species, and C–C coupled intermediate species. At low coverages, the Au/Ti interface and numerous grain boundaries in thicker films are assumed to act as active sites for C–C coupling.

It is worth reiterating that Au/TiO_x catalysts have been widely used in various catalytic reactions, including CO_2 reduction, producing mainly H_2 , CO, and CH_4 [10,16–28]. However, there are no reports on the use of Au/Ti catalysts for electrochemical F–T synthesis of long-chain hydrocarbons. In F–T synthesis conditions, the surface CO and H species play a crucial role, and the adsorption abilities of these species on the catalyst surface are of utmost importance. This study investigates the role of the engineered Au and Ti interface in this context.

4. Conclusions

In conclusion, we tested EC CO_2 and CO reductions over Au/Ti electrodes and successfully demonstrated the production of long-chain hydrocarbons of C_nH_{2n} and $\text{C}_n\text{H}_{2n+2}$, $n=2-7$ for the first time. The experiments were carried out over interface-engineered Au/Ti electrodes in CO_2 - and CO-saturated KHCO_3 and $\text{K}_2\text{HPO}_4/\text{KH}_2\text{PO}_4$ buffer electrolytes using the mimicked EC F–T synthesis method. In ambient pressure and temperature conditions, H^* was achieved via $\text{H}^+ + \text{e}^- \rightarrow \text{H}^*$. Surface *CO was formed directly via $\text{CO (g)} \rightarrow \text{*CO}$ in CO-saturated

condition and indirectly via $\text{CO}_2(\text{g}) + \text{H}^+ + \text{e}^- \rightarrow \text{*COOH} \rightarrow \text{*CO}$ in CO_2 -saturated condition. It was found that the initial adsorption of CO_2 and CO played a significant role in hydrocarbon production, and their adsorption was dependent on the Au/Ti interface. Therefore, the engineered interface between Au and Ti plays a crucial role in hydrocarbon production. In a CO_2 -saturated 0.1 M KHCO_3 condition, the FE of CO was observed to be 37.5% over Au(640 s)/Ti, while CO production was substantially diminished in NaHCO_3 , phosphate, and highly-concentrated KHCO_3 electrolytes. CH_4 and C_{2-7} hydrocarbons were substantially increased in KHCO_3 with a high concentration and phosphate electrolytes. In CO_2 -saturated KHCO_3 condition, Au(10 s)/Ti showed the highest hydrocarbon productions, with less CH_4 produced but higher C_{2-7} hydrocarbons, due to CO adsorption enhancement at the interface of Au and Ti. The Au(640 s)/Ti electrode showed the highest hydrocarbon productions in CO_2 -saturated phosphate. In CO-saturated conditions, the Au/Ti electrode showed higher hydrocarbon production compared to bare Au due to less CO adsorption on the bare Au surface. The $\text{C}_n\text{H}_{2n+2}/\text{C}_n\text{H}_{2n}$ ratios were found to be higher than 1.5, increasing with increasing overlayer Au and decreasing with increasing applied potential, indicating a higher production of alkanes than the corresponding alkenes. On the basis of ASF weight distribution plots, a surface C–C coupling polymerization mechanism was proposed with hydrogenation and dehydration starting from surface *CO and H^* . Polymerization paths included insertions of surface *CH_x and *CO species. Overall, the demonstration tests in CO_2 and CO-saturated conditions using Au/Ti electrodes provide useful information on the development of mimicked F–T synthesis by electrochemistry for long-chain hydrocarbon energy fuels.

CRediT authorship contribution statement

Young Jun Kim: Methodology, Investigation, Validation, Data curation, Formal analysis, Investigation, Writing – original draft. **Ju Young Maeng:** Investigation, Validation, Data curation, Formal analysis. **Seon Young Hwang:** Investigation, Validation, Data curation, Formal analysis. **Choong Kyun Rhee:** Supervision, Conceptualization, Reviewing. **Youngku Sohn:** Supervision, Conceptualization, Resources, Validation, Writing – original draft, Writing – review & editing, Project administration, Funding acquisition.

Declaration of Competing Interest

The authors declare that they have no known competing financial interests or personal relationships that could have appeared to influence the work reported in this paper.

Data availability

Data will be made available on request.

Acknowledgement

This work was supported financially by National Research Foundation of Korea (NRF) grant funded by the Korea government (MEST) (2021R1A2C2003929).

Appendix A. Supporting information

Supplementary data associated with this article can be found in the online version at doi:10.1016/j.apcatb.2023.123017.

References

- [1] Y. Lu, Z. Zhang, H. Wang, Y. Wang, Toward efficient single-atom catalysts for renewable fuels and chemicals production from biomass and CO_2 , Appl. Catal. B Environ. 292 (2021) 120162–120199, <https://doi.org/10.1016/j.apcatb.2021.120162>.

- [2] M.T. Tang, H. Peng, P.S. Lamoureux, M. Bajdich, F. Abild-Pedersen, From electricity to fuels: descriptors for C1 selectivity in electrochemical CO₂ reduction, *Appl. Catal. B Environ.* 279 (2020), 119384, <https://doi.org/10.1016/j.apcatb.2020.119384>.
- [3] G. Wang, J. Chen, Y. Ding, P. Cai, L. Yi, Y. Li, et al., Electrocatalysis for CO₂ conversion: from fundamentals to value-added products, *Chem. Soc. Rev.* 50 (2021) 4993–5061, <https://doi.org/10.1039/D0CS00071J>.
- [4] S. Overa, B.H. Ko, Y. Zhao, F. Jiao, Electrochemical approaches for CO₂ conversion to chemicals: a journey toward practical applications, *Acc. Chem. Res.* 55 (2022) 638–648, <https://doi.org/10.1021/acs.accounts.1c00674>.
- [5] Q. Fan, M. Zhang, M. Jia, S. Liu, J. Qiu, Z. Sun, Electrochemical CO₂ reduction to C₂₊ species: Heterogeneous electrocatalysts, reaction pathways, and optimization strategies, *Mater. Today Energy* 10 (2018) 280–301, <https://doi.org/10.1016/j.mtener.2018.10.003>.
- [6] Y. Yang, S. Ajmal, X. Zheng, L. Zhang, Efficient nanomaterials for harvesting clean fuels from electrochemical and photoelectrochemical CO₂ reduction, *Sustain. Energ. Fuels* 2 (2018) 510–537, <https://doi.org/10.1039/C7SE00371D>.
- [7] S. Nitopi, E. Bertheussen, S.B. Scott, X. Liu, A.K. Engstfeld, S. Horch, B. Segar, I.E. L. Stephens, K. Chan, C. Hahn, J.K. Nørskov, T.F. Jaramillo, I. Chorkendorff, Progress and perspectives of electrochemical CO₂ reduction on copper in aqueous electrolyte, *Chem. Rev.* 119 (2019) 7610–7672, <https://doi.org/10.1021/acs.chemrev.8b00705>.
- [8] Q. Lu, F. Jiao, Electrochemical CO₂ reduction: electrocatalyst, reaction mechanism, and process engineering, *Nano Energy* 29 (2016) 439–456, <https://doi.org/10.1016/j.nanoen.2016.04.009>.
- [9] X. Lv, Q. Liu, J. Wang, X. Wu, X. Li, Y. Yang, J. Yan, A. Wu, H.B. Wu, Grain refining enables mixed Cu⁺/Cu⁰ states for CO₂ electroreduction to C₂₊ products at high current density, *Appl. Catal. B Environ.* 324 (2023), 122272, <https://doi.org/10.1016/j.apcatb.2022.122272>.
- [10] Y. Sohn, W. Huang, F. Taghipour, Recent progress and perspectives in the photocatalytic CO₂ reduction of Ti-oxide-based nanomaterials, *Appl. Surf. Sci.* 396 (2017) 1696–1711, <https://doi.org/10.1016/j.apsusc.2016.11.240>.
- [11] X. Wang, Q. Chen, Y. Zhou, H. Li, J. Fu, M. Liu, Cu-based bimetallic catalysts for CO₂ reduction reaction, *Adv. Sens. Energy Mater.* 1 (2022), 100023, <https://doi.org/10.1002/aenm.202270001>.
- [12] B. Sun, M. Dai, S. Cai, H. Cheng, K. Song, Y. Yu, H. Hu, Challenges and strategies towards copper-based catalysts for enhanced electrochemical CO₂ reduction to multi-carbon products, *Fuel* 332 (2023), 126114, <https://doi.org/10.1016/j.fuel.2022.126114>.
- [13] H. Xie, T. Wang, J. Liang, Q. Li, S. Sun, Cu-based nanocatalysts for electrochemical reduction of CO₂, *Nano Today* 21 (2018) 41–54, <https://doi.org/10.1016/j.nantod.2018.05.001>.
- [14] T. Ahmad, S. Liu, M. Sajid, K. Li, M. Ali, L. Liu, et al., Electrochemical CO₂ reduction to C₂₊ products using Cu-based electrocatalysts: a review, *Nano Res. Energy* 1 (2022), e9120021, <https://doi.org/10.26599/NRE.2022.9120021>.
- [15] P. Chen, Y. Wu, T.E. Rufford, L. Wang, G. Wang, Z. Wang, Organic molecules involved in Cu-based electrocatalysts for selective CO₂ reduction to C₂₊ products, *Mater. Today Chem.* 27 (2023), 101328, <https://doi.org/10.1016/j.mtchem.2022.101328>.
- [16] A. Pougin, G. Dodekatos, M. Dilla, H. Teyssie, J. Strunk, Au@TiO₂ core-shell composites for the photocatalytic reduction of CO₂, *Chem. Eur. J.* 24 (2018) 12416–12425, <https://doi.org/10.1002/chem.201801796>.
- [17] R. Wang, J. Shen, K. Sun, H. Tang, Q. Liu, Enhancement in photocatalytic activity of CO₂ reduction to CH₄ by OD/2D Au/TiO₂ plasmon heterojunction, *Appl. Surf. Sci.* 493 (2019) 1142–1149, <https://doi.org/10.1016/j.apsusc.2019.07.121>.
- [18] X. Wanf, X. Xiaoni, Y. Wang, X. Li, H. Hunag, X. Zhang, Nano-Au-modified TiO₂ grown on dendritic porous silica particles for enhanced CO₂ photoreduction, *Microporous Mesoporous Mater.* 310 (2021), 110635, <https://doi.org/10.1016/j.micromeso.2020.110635>.
- [19] B. Mei, A. Pougin, J. Strunk, Influence of photodeposited gold nanoparticles on the photocatalytic activity of titanate species in the reduction of CO₂ to hydrocarbons, *J. Catal.* 306 (2013) 184–189, <https://doi.org/10.1016/j.jcat.2013.06.027>.
- [20] (a) P. Martínez Molina, N. Meulendijks, M. Xu, M.A. Verheijen, T. den Hartog, P. Buskens, F. Sastre, Low temperature sunlight-powered reduction of CO₂ to CO using a plasmonic Au/TiO₂ nanocatalyst, *ChemCatChem* 13 (2021) 4507–4513, <https://doi.org/10.1002/cctc.202100699>;
(b) K. Wang, J.B. Lu, Y. Lu, C.H. Lau, Y. Zheng, X.F. Fan, Unravelling the C-C coupling in CO₂ photocatalytic reduction with H₂O on Au/TiO_{2-x}: combination of plasmonic excitation and oxygen vacancy, *Appl. Catal. B Environ.* 292 (2021) 120147–120160, <https://doi.org/10.1016/j.apcatb.2021.120147>.
- [21] C. Wang, Y. Zhao, H. Xu, Y. Li, Y. Wei, J. Liu, Z. Zhao, Efficient Z-scheme photocatalysts of ultrathin g-C₃N₄-wrapped Au/TiO₂-nanocrystals for enhanced visible-light-driven conversion of CO₂ with H₂O, *Appl. Catal. B Environ.* 263 (2020), 118314, <https://doi.org/10.1016/j.apcatb.2019.118314>.
- [22] F. Raziq, L. Sun, Y. Wang, X. Zhang, M. Humayun, S. Ali, L. Bai, Y. Qu, H. Yu, L. Jing, Synthesis of large surface-area g-C₃N₄ comodified with MnO_x and Au-TiO₂ as efficient visible-light photocatalysts for fuel production, *Adv. Energy Mater.* 8 (2017) 1701580, <https://doi.org/10.1002/aenm.201701580>.
- [23] M. Tahir, Synergistic effect in MMT-dispersed Au/TiO₂ monolithic nanocatalyst for plasmon-absorption and metallic interband transitions dynamic CO₂ photo-reduction to CO, *Appl. Catal. B Environ.* 219 (2017) 329–343, <https://doi.org/10.1016/j.apcatb.2017.07.062>.
- [24] X. Jiang, J. Huang, Z. Bi, W. Ni, G. Gurzadyan, Y. Zhu, Z. Zhang, Plasmonic active “hot spots”-confined photocatalytic CO₂ reduction with high selectivity for CH₄ production, *Adv. Mater.* 34 (2022) 2109330, <https://doi.org/10.1002/adma.202109330>.
- [25] S. Zeng, E. Vahidzadeh, C.G. VanEssen, P. Kar, R. Kisslinger, A. Goswami, Y. Zhang, N. Mandi, S. Riddell, A.E. Kobryn, S. Gusarov, P. Kumar, K. Shankar, Optical control of selectivity of high rate CO₂ photoreduction via interband hot electron Z-scheme reaction pathways in Au-TiO₂ plasmonic photonic crystal photocatalyst, *Appl. Catal. B Environ.* 267 (2020), 118644, <https://doi.org/10.1016/j.apcatb.2020.118644>.
- [26] M.N. Hossain, R.M. Choueiri, S. Abner, L.D. Chen, A. Chen, Electrochemical reduction of carbon dioxide at TiO₂/Au nanocomposites, *ACS Appl. Mater. Interfaces* 14 (2022) 51889–51899, <https://doi.org/10.1021/acsami.2c14368>.
- [27] G.Y. Liu, P.R. Narangari, Q.T. Trinh, W.G. Tu, M. Kraft, H.H. Tan, C. Jagadish, T. S. Choksi, J.W. Ager, S. Karuturi, R. Xu, Manipulating intermediates at the Au-TiO₂ interface over InP nanopillar array for photoelectrochemical CO₂ reduction, *ACS Catal.* 11 (2021) 11416–11428, <https://doi.org/10.1021/acscatal.1c02043>.
- [28] C. Li, T. Wang, B. Liu, M. Chen, A. Li, G. Zhang, Photoelectrochemical CO₂ reduction to adjustable syngas on grain-boundary-mediated a-Si/TiO₂/Au photocathodes with low onset potentials, *Energy Environ. Sci.* 12 (2019) 923–928, <https://doi.org/10.1039/C8EE02768D>.
- [29] M. Cho, J.T. Song, S. Back, Y. Jung, J. Oh, The role of adsorbed CN and Cl on an Au electrode for electrochemical CO₂ reduction, *ACS Catal.* 8 (2018) 1178–1185, <https://doi.org/10.1021/acscatal.7b03449>.
- [30] Y. Fang, J.C. Flake, Electrochemical reduction of CO₂ at functionalized Au electrodes, *J. Am. Chem. Soc.* 139 (2017) 3399–3405, <https://doi.org/10.1021/jacs.6b11023>.
- [31] G. Marcandalli, A. Goyal, M.T.M. Koper, Electrolyte effects on the Faradaic efficiency of CO₂ reduction to CO on a gold electrode, *ACS Catal.* 11 (2021) 4936–4945, <https://doi.org/10.1021/acscatal.1c00272>.
- [32] E.R. Cave, J.H. Montoya, K.P. Kuhl, D.N. Abram, T. Hatsukade, C. Shi, Electrochemical CO₂ reduction on Au surfaces: mechanistic aspects regarding the formation of major and minor products, *Phys. Chem. Chem. Phys.* 19 (2017) 15856–15863, <https://doi.org/10.1039/C7CP02855E>.
- [33] N. Todoroki, H. Tei, H. Tsurumaki, T. Miyakawa, T. Inoue, T. Wadayama, Surface atomic arrangement dependence of electrochemical CO₂ reduction on gold: online electrochemical mass spectrometric study on low-index Au(hkl) surfaces, *ACS Catal.* 9 (2019) 1383–1388, <https://doi.org/10.1021/acscatal.8b04852>.
- [34] H. Eidsvåg, S. Bentouba, P. Vajeeston, S. Yohi, D. Velauthapillai, TiO₂ as a photocatalyst for water splitting—an experimental and theoretical review, *Molecules* 26 (2021) 1687, <https://doi.org/10.3390/molecules26061687>.
- [35] M. Ni, M.K.H. Leung, D.Y.C. Leung, K. Sumathy, A review and recent developments in photocatalytic water-splitting using TiO₂ for hydrogen production, *Renew. Sustain. Energy Rev.* 11 (2007) 401–425, <https://doi.org/10.1016/j.rser.2005.01.009>.
- [36] H. Mahmoudi, M. Mahmoudi, O. Doudstard, H. Jahangiri, A. Tsolakis, S. Gu, M. L. Wyszynski, A review of Fischer Tropsch synthesis process, mechanism, surface chemistry and catalyst formulation, *Biofuels Eng.* 2 (2017) 11–31, <https://doi.org/10.1515/bfuel-2017-0002>.
- [37] O.O. James, B. Chowdhury, M.A. Mesubi, S. Maity, Reflections on the chemistry of the Fischer–Tropsch synthesis, *RSC Adv.* 2 (2012) 7347–7366, <https://doi.org/10.1039/C2RA20519J>.
- [38] W.X. Ye, X.L. Guo, T.L. Ma, A review on electrochemical synthesized copper-based catalysts for electrochemical reduction of CO₂ to C₂₊ products, *Chem. Eng. J.* 414 (2021), 128825, <https://doi.org/10.1016/j.cej.2021.128825>.
- [39] S. Liu, B. Zhang, L. Zhang, J. Sun, Rational design strategies of Cu-based electrocatalysts for CO₂ electroreduction to C₂ products, *J. Energy Chem.* 71 (2022) 63–68, <https://doi.org/10.1016/j.jechem.2022.03.041>.
- [40] H. Shibata, J.A. Moulijn, G. Mul, Enabling electrocatalytic Fischer–Tropsch synthesis from carbon dioxide over copper-based electrodes, *Catal. Lett.* 186 (2008) 186–192, <https://doi.org/10.1007/s10562-008-9488-3>.
- [41] R. Kortlever, I. Peters, C. Balemans, R. Kas, Y. Kwon, G. Mul, M.T.M. Koper, Palladium–gold catalyst for the electrochemical reduction of CO₂ to C₁–C₅ hydrocarbons, *Chem. Commun.* 52 (2016) 10229–10232, <https://doi.org/10.1039/C6CC03717H>.
- [42] M. Jouny, G.S. Hutchings, F. Jiao, Carbon monoxide electroreduction as an emerging platform for carbon utilization, *Nat. Catal.* 2 (2019) 1062–1070, <https://doi.org/10.1038/s41929-019-0388-2>.
- [43] Z. Liu, J. Cao, B. Wu, L. Qian, A. Guan, C. Yang, X. Lv, L. Zhang, G. Zheng, Surface energy tuning on Cu/NC catalysts for CO electroreduction, *ACS Catal.* 12 (2022) 12555–12562, <https://doi.org/10.1021/acscatal.2c02261>.
- [44] C.W. Li, J. Ciston, M. Kanan, W. Electroreduction of carbon monoxide to liquid fuel on oxide-derived nanocrystalline copper, *Nature* 508 (2012) 504–507, <https://doi.org/10.1038/nature13249>.
- [45] H. Zhang, J. Li, M.J. Cheng, Q. Lu, CO electroreduction: current development and understanding of Cu-based catalysts, *ACS Catal.* 9 (2019) 49–65, <https://doi.org/10.1021/acscatal.8b03780>.
- [46] Y. Zhang, J.-X. Liu, K. Qian, A. Jia, D. Li, L. Shi, Structure–sensitivity of Au–TiO₂ strong metal–support interaction, *Angew. Chem., Int. Ed.* 60 (2021) 12074–12081, <https://doi.org/10.1002/anie.202101928>.
- [47] A. Tavakoli, M. Sohrabi, A. Kargari, Application of anderson–schulz–flory (asf) equation in the product distribution of slurry phase ft synthesis with nanosized iron catalysts, *Chem. Eng. J.* 136 (2008) 358–363, <https://doi.org/10.1016/j.cej.2007.04.017>.
- [48] S.J. Park, M.H. Joo, J.Y. Maeng, C.K. Rhee, J.G. Kang, Y. Sohn, Electrochemical Ce³⁺/Ce⁴⁺ and Eu²⁺/Eu³⁺ interconversion, complexation, and electrochemical CO₂ reduction on thio-terpyridyl-derivatized Au electrodes, *Appl. Surf. Sci.* 576 (2022), 151793, <https://doi.org/10.1016/j.apsusc.2021.151793>.

- [49] M.D. Calisir, M. Gungor, A. Demir, A. Kilic, M.M. Khan, Nitrogen-doped TiO₂ fibers for visible-light-induced photocatalytic activities, *Ceram. Int.* 46 (2020) 16743–16753, <https://doi.org/10.1016/j.ceramint.2020.03.250>.
- [50] N. Roy, Y. Sohn, K.T. Leung, D. Pradhan, Engineered electronic states of transition metal doped TiO₂ nanocrystals for low overpotential oxygen evolution reaction, *J. Phys. Chem. C* 118 (2014) 29499–29506, <https://doi.org/10.1021/jp508445t>.
- [51] J.G. Kang, Y. Sohn, Interfacial nature of Ag nanoparticles supported on TiO₂ photocatalysts, *J. Mater. Sci.* 47 (2012) 824–832, <https://doi.org/10.1007/s10853-011-5860-6>.
- [52] C.J. Powell, A. Jablonski, NIST Electron Inelastic-mean-free-path Database - Version 1.2, National Institute of Standards and Technology, Gaithersburg, MD, 2010. (<https://www.nist.gov/srd/nist-standard-reference-database-71>).
- [53] P.J. Cumpson, The thickogram: a method for easy film thickness measurement in XPS (2000), *Surf. Interface Anal.* 29 (2000) 403–406, [https://doi.org/10.1002/1096-9918\(200006\)29:6<403::AID-SIA884>3.0.CO;2-8](https://doi.org/10.1002/1096-9918(200006)29:6<403::AID-SIA884>3.0.CO;2-8).
- [54] (<http://www.xpsfitting.com/2009/04/relative-sensitivity-factors-rsf.html#54>).
- [55] W. Liu, P. Zhai, A. Li, et al., Electrochemical CO₂ reduction to ethylene by ultrathin CuO nanoplate arrays, *Nat. Commun.* 13 (2022) 1877, <https://doi.org/10.1038/s41467-022-29428-9>.
- [56] Y. Jiang, D. Zhong, L. Wang, J. Li, G. Hao, J. Li, Q. Zhao, Roughness effect of Cu on electrocatalytic CO₂ reduction towards C₂H₄, *Chem. Asian J.* 17 (2022), e202200380, <https://doi.org/10.1002/asia.202200380>.
- [57] M. Schreier, Y. Yoon, M.N. Jackson, Y. Surendranath, Competition between H and CO for active sites governs copper-mediated electrosynthesis of hydrocarbon fuels, *Angew. Chem. Int. Ed.* 57 (2018) 10221–10225, <https://doi.org/10.1002/anie.201806051>.
- [58] T. Cheng, H. Xiao, W.A. Goddard III, Reaction mechanisms for the electrochemical reduction of CO₂ to CO and formate on the Cu(100) surface at 298 K from quantum mechanics free energy calculations with explicit water, *J. Am. Chem. Soc.* 138 (2016) 13802–13805, <https://doi.org/10.1021/jacs.6b08534>.
- [59] J.Y. Maeng, J.H. Yang, H.J. Jang, M.H. Joo, Y.J. Kim, C.K. Rhee, Y. Sohn, Electrocatalytic syngas and photocatalytic long-chain hydrocarbon productions by CO₂ reduction over ZnO and Zn-based electrodes, *Appl. Surf. Sci.* 609 (2023), 155349, <https://doi.org/10.1016/j.apsusc.2022.155349>.
- [60] H.J. Jang, J.H. Yang, J.Y. Maeng, Y.J. Kim, C.K. Rhee, Y. Sohn, Electrochemical CO₂ reduction over Pb electrodes modified with group 10, 11, and 14 elements, *Appl. Surf. Sci.* 604 (2022), 154438, <https://doi.org/10.1016/j.apsusc.2022.154438>.
- [61] H.J. Jang, J.Y. Maeng, Y.J. Kim, I. Yoon, C.W. Myung, C.K. Rhee, Y. Sohn, Electrocatalytic CO₂ reduction reaction over group 15 bismuth and antimony film electrodes: What makes difference, *J. CO₂ Util.* 64 (2022), 102202, <https://doi.org/10.1016/j.jcou.2022.102202>.
- [62] F. Abild-Pedersen, M.P. Andersson, CO adsorption energies on metals with correction for high coordination adsorption sites – A density functional study, *Surf. Sci.* 601 (2007) 1747–1753, <https://doi.org/10.1016/j.susc.2007.01.052>.
- [63] Y. Zhao, C. Cui, J. Han, H. Wang, X. Zhu, Q. Ge, Direct C–C coupling of CO₂ and the methyl group from CH₄ activation through facile insertion of CO₂ into Zn–CH₃ σ-bond, *J. Am. Chem. Soc.* 138 (2016) 10191–10198, <https://doi.org/10.1021/jacs.6b04446>.
- [64] B. Todic, W. Ma, G. Jacobs, B.H. Davis, D.B. Bukur, CO-insertion mechanism based kinetic model of the Fischer–Tropsch synthesis reaction over Re-promoted Co catalyst, *Catal. Today* 228 (2016) 32–39, <https://doi.org/10.1016/j.cattod.2013.08.008>.
- [65] Y. Zhou, A.J. Martín, F. Dattila, S. Xi, N. López, J. Pérez-Ramírez, B.S. Yeo, Long-chain hydrocarbons by CO₂ electroreduction using polarized nickel catalysts, *Nat. Catal.* 5 (2022) 545–554, <https://doi.org/10.1038/s41929-022-00803-5>.